Journal Pre-proofs

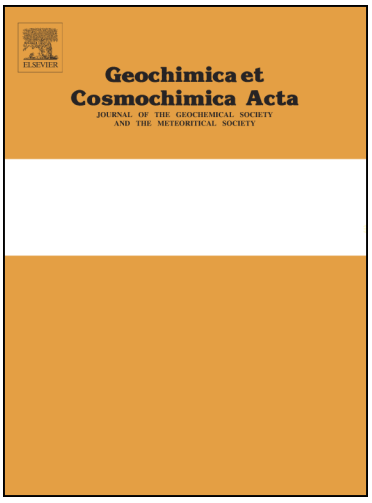

Early diagenesis of iron and sulfur in Bornholm Basin sediments: the role of near-surface pyrite formation

Jiarui Liu, André Pellerin, Gilad Antler, Sabine Kasten, Alyssa J. Findlay, Ingrid Dohrmann, Hans Røy, Alexandra V. Turchyn, Bo Barker Jørgense

PII: S0016-7037(20)30363-X
DOI: https://doi.org/10.1016/j.gca.2020.06.003
Reference: GCA 11795

To appear in: *Geochimica et Cosmochimica Acta*

Received Date: 13 March 2020
Revised Date: 14 May 2020
Accepted Date: 3 June 2020

Please cite this article as: Liu, J., Pellerin, A., Antler, G., Kasten, S., Findlay, A.J., Dohrmann, I., Røy, H., Turchyn, A.V., Barker Jørgense, B., Early diagenesis of iron and sulfur in Bornholm Basin sediments: the role of near-surface pyrite formation, *Geochimica et Cosmochimica Acta* (2020), doi: https://doi.org/10.1016/j.gca.2020.06.003

Early diagenesis of iron and sulfur in Bornholm Basin sediments: the role of near-surface pyrite formation

Jiarui Liu [a, b, *], André Pellerin [a, c], Gilad Antler [c, d], Sabine Kasten [e, f], Alyssa J. Findlay [a], Ingrid Dohrmann [e], Hans Røy [a], Alexandra V. Turchyn [g], Bo Barker Jørgensen [a]

[a] Section for Microbiology, Department of Biology, Aarhus University, 8000 Aarhus C, Denmark

[b] Department of Earth, Planetary and Space Sciences, University of California, Los Angeles, CA 90095, USA

[c] Department of Geological and Environmental Sciences, Ben-Gurion University of the Negev, Beersheba 84105, Israel

[d] The Interuniversity Institute for Marine Sciences, Eilat 88103, Israel

[e] Alfred Wegener Institute Helmholtz Centre for Polar and Marine Research, 27570 Bremerhaven, Germany

[f] Faculty of Geosciences, University of Bremen, 28359 Bremen, Germany

[g] Department of Earth Sciences, University of Cambridge, Cambridge CB2 3EQ, UK

[*] Corresponding author. *E-mail address:* jiaruiliu@ucla.edu (J. Liu).

Keywords: Baltic Sea; biogeochemical sulfur cycling; degree of pyritization; marine sediments; solid-phase sulfur; sulfur isotopes

Abstract

Pyrite formation in marine sedimentary environments plays a key role in the global biogeochemical cycles of carbon, sulfur and iron, regulating Earth's surface redox balance over geological time scales. The sulfur isotopic composition of pyrite is one of the major geochemical tools for investigating early diagenetic processes in modern marine sediments and substantive changes to the Earth's surface environment in ancient sedimentary rocks. We studied sulfur–iron diagenesis and the sulfur isotopic evolution in sediments of the Bornholm Basin, southwestern Baltic Sea, to track the formation of pyrite in the near-surface sediments. Pyrite accumulation is observed with depth over the uppermost 100 cm before the extent of pyritization of the highly reactive iron pool (Fe_{py}/Fe_{HR}) stays constant at ca. 0.9, suggesting that the use of a single iron-speciation parameter as a proxy for anoxic and sulfidic conditions needs to be supported by other independent indicators in sedimentary records. Stable sulfur isotopic analysis demonstrates that the bulk pools of elemental sulfur and iron monosulfide do not exchange isotopes completely with aqueous sulfide. We suggest that the reactions with polysulfide and aqueous sulfide are probably restricted to the surface of the solid-phase sulfur and iron-sulfur aggregates. Although pyrite is growing throughout the uppermost sediment column, the pyrite at depth has a sulfur isotopic composition similar to that of pyrite that formed near the sediment surface. To understand the isotopic discrepancy between pyrite and aqueous sulfide in the deeper sediments, we developed a simple diagenetic model, which reproduces the observed sulfur isotopic composition of pyrite well. Our results suggest that much of the pyrite is rapidly formed near the sediment–water interface, and its $\delta^{34}S$ is not as influenced by the ^{34}S-enriched pool of aqueous sulfide in the deeper part of the sediment, allowing ^{32}S-enriched pyrite to be preserved in deeper sediments. This near-surface diagenesis and the associated isotopic pattern are possibly of relevance for many marine sediments with high organic matter content, and high aqueous sulfide but low reactive iron availability. Moreover, our sulfur isotopic data demonstrate that extremely slow pyritization is ongoing in the deep lacustrine clay sediments. These results have implications for the interpretation of sulfur–iron geochemical data in both modern and ancient settings as well as for improving reconstructions of ancient depositional environments and a better understanding of the marine sulfur cycle throughout Earth's history.

1. INTRODUCTION

The biogeochemical sulfur cycle within marine sediments integrates the microbial activity of diverse metabolic pathways. Dissimilatory sulfate reduction by anaerobic microorganisms dominates organic matter mineralization in the contemporary anoxic seabed (Jørgensen, 1982; Jørgensen and Kasten, 2006). The vast majority of sulfide produced by sulfate reduction, however, is reoxidized back to sulfate by either geochemical or microbial reactions involving several sulfur intermediates (e.g., Zopfi et al., 2004; Rickard, 2012b). A fraction of the aqueous sulfide is scavenged by reactive iron and is ultimately buried as pyrite (FeS_2) in the sediment, representing the dominant mechanism for sulfur burial in marine environments (Hensen et al., 2003; Bottrell and Newton, 2006; Fike et al., 2015). Very generally, the formation of pyrite can be divided into two steps: the reaction of aqueous sulfide to metastable iron monosulfide (FeS) and the reaction of iron monosulfide to pyrite (Berner, 1984; Rickard and Luther, 2007). The former reaction is relatively fast in aqueous solutions, while the latter one involves multiple complex pathways with diverse reaction rates (e.g., Rickard, 1995; Rickard and Morse, 2005; Rickard and Luther, 2007). Although several pathways for the reaction of iron monosulfide to pyrite have been proposed, only two reaction pathways have been determined by stoichiometry, kinetics and mechanism: the reaction between polysulfide and iron monosulfide ("polysulfide pathway"; Rickard, 1975; Luther, 1991) and the reaction between H_2S and iron monosulfide ("H_2S pathway"; Rickard, 1997; Thiel et al., 2019). Polysulfides are formed via the reaction between aqueous sulfide and elemental sulfur (cf. Findlay, 2016), while elemental sulfur is one of the major intermediate products of sulfide oxidation (e.g., Zopfi et al., 2004), increasing the complexity of geochemical processes that form pyrite.

The redox transformations of sulfur within marine sediments are typically associated with distinctive stable isotopic fractionations of the various sulfur species. It has been shown that dissimilatory sulfate reduction, the disproportionation of intermediate-valence state sulfur species and bacterial sulfide oxidation can generate pronounced enrichments or depletions in ^{34}S (e.g., Canfield and Thamdrup, 1994; Sim et al., 2011; Pellerin et al., 2019). Consequently, stable sulfur isotopic analysis ($\delta^{34}S$) has provided unprecedented

insight into the operation of the biogeochemical sulfur cycle, such as determining both rates and pathways of microbial reactions (Sim et al., 2011; Leavitt et al., 2013; Jørgensen et al., 2019). Sedimentary pyrite is also ubiquitous in ancient sedimentary rocks. As such, the $\delta^{34}S$ of pyrite preserved in the sedimentary record has been suggested to be fundamental to the reconstruction and understanding of changes in Earth's surface environment over geological time, including the oxygenation of the atmosphere and oceans, and episodes of biological evolution and mass extinction (e.g., Berner, 1984; Canfield, 2001; Fike et al., 2015).

The above inferences, however, assume that changes in the $\delta^{34}S$ of pyrite reflect the large-scale temporal changes in the global biogeochemical sulfur cycle. Field studies of modern marine sediments have shown that the $\delta^{34}S$ of pyrite can be influenced by several factors, including diagenetic pyrite formation at the sulfate–methane transition (SMT) and changes in local depositional conditions (e.g., Borowski et al., 2013; Fike et al., 2015; Pasquier et al., 2017; Riedinger et al., 2017). For example, enhanced pyrite formation at the SMT tends to enrich sedimentary pyrite in the ^{34}S isotope (Borowski et al., 2013; Lin et al., 2016; Turchyn et al., 2016; Riedinger et al., 2017; Liu et al., 2020). Recent studies have found that changes in the sulfur isotopic composition in sedimentary pyrite correspond to changes in local environmental conditions and related variations in sedimentation rate (Pasquier et al., 2017; Liu et al., 2019). The marine settings studied are characterized by low/moderate contents of organic matter but high availability of reactive iron, providing ideal conditions for pyrite formation. In contrast, high organic carbon contents but low reactive iron availability may limit pyrite formation within marine sediments. For example, Formolo and Lyons (2013) found that most pyrite formation appeared to be very early and was limited by the availability of reactive iron phases in cold seep environments. Content and type of organic matter and availability of reactive iron, in turn, control sulfide production and consumption, respectively (Berner, 1984; Middelburg, 1991; Kasten et al., 1998; Fu et al., 2008; Roberts, 2015; Shawar et al., 2018). Thus, organic matter content and availability of reactive iron and aqueous sulfide have the potential to influence the sulfur isotopic composition of pyrite, in addition to changes in sedimentation rate or changes in other local environmental conditions. Given the importance of sedimentary pyrite in the interpretation of the evolution of Earth's

surface environment, a thorough understanding of the role of organic matter, reactive iron and aqueous sulfide in the pyrite $\delta^{34}S$ values will vastly improve our ability to interpret the geological record and to more adequately test long-standing hypotheses linking ocean chemistry, climate and the evolution of the biosphere.

In this study, we collected multiple sediment cores from the Bornholm Basin (Baltic Sea) with high organic matter content, and high aqueous sulfide but low reactive iron availability in Holocene marine sediments. We determined the sulfur and iron geochemistry of both porewater and solid-phase sediments with high stratigraphic resolution. Our data show the transformation of iron oxides to iron sulfides. The sulfur isotopic data are used to investigate the potential for sulfur isotope exchange among various valence state sulfur species. In addition, a diagenetic model is developed to understand the evolution of the sulfur isotopic signature of pyrite in these near-surface sediments. These isotopic records and modeling from the Bornholm Basin sediments provide new insight into the isotope geochemistry of pyrite in both contemporary and ancient sedimentary environments.

2. MATERIALS AND METHODS

2.1. Site description

The Bornholm Basin is located in the southwestern Baltic Sea, with sediments at water depths of around 75–96 m. The sediment stratigraphy and lithology are controlled by sediment accumulation since the last deglaciation, when the Bornholm basin was a freshwater lake. Here, postglacial sea-level rise resulted in the accumulation of organic-rich, brackish-marine sediments overlying organic-poor lacustrine sediments. Sediment cores were taken in the Bornholm Basin during a research cruise in 2016 on the R/V *Aurora* (Fig. 1). Guided by preceding exploratory cruises, we carefully chose study sites according to their Holocene Mud Layer (HML) thickness and organic matter burial history (Table 1). Each site was sampled with a gravity corer (9 m in length) and a Rumohr corer (1 m in length). We present data from three sites (BB01, BB02 and BB05) to study sulfur–iron geochemistry in the Bornholm Basin with comprehensive sulfur–iron concentration and sulfur isotopic data.

2.2. Porewater sampling and analyses

Gravity cores were cut into sections and capped immediately on board. Porewater sampling and analyses procedures are as described in Beulig et al. (2018) and Pellerin et al. (2018). In brief, sediments for methane concentration analysis were taken through small holes drilled in the core liner and immediately transferred to glass vials containing a saturated NaCl solution. The vials were then crimp sealed, vigorously shaken and stored upside down at −20 °C. An improved procedure for porewater retrieval was adopted to minimize the potential of sulfate contamination during sampling (Pellerin et al., 2018). Rhizon soil moisture samplers (Rhizosphere Research Products) were inserted into the sediments and immediately connected to an evacuated syringe. The first 1–2 mL was discarded, after which a Vacutainer was connected to collect pore fluid. The sulfate samples were bubbled with humidified CO_2 gas to remove H_2S, and subsequently stored at 4 °C until analysis. The samples for sulfide concentration were fixed with 5% zinc acetate solution and

frozen until analysis. Samples for dissolved ferrous iron and barium concentrations were diluted 10 times with 0.01 N trace metal grade nitric acid and subsequently stored at 4 °C until analysis.

Methane in the headspace was analyzed on a gas chromatograph (SRI 310C; SRI Instruments) equipped with a packed silica gel column and a flame ionization detector. Sulfate was analyzed by ion chromatography on a Dionex system using an AG-18/AS-18 column with a KOH eluent. Aqueous sulfide ($\sum H_2S$) was determined spectrophotometrically using the methylene blue method (Cline, 1969). Dissolved ferrous iron and barium were analyzed by inductively coupled plasma mass spectrometry (ICP-MS) using a Thermo Fisher Scientific Element 2 ICP-MS at the Alfred Wegener Institute Helmholtz Centre for Polar and Marine Research (AWI).

2.3. Solid-phase sediment sampling and analyses

Sediments in gravity-core subsections were sampled by cutting windows in the core liner while sediments in Rumor cores were sampled with a core extruder. Solid-phase samples were taken with a cutoff syringe, sealed with Parafilm, and immediately frozen at −20 °C under anoxic condition. Frozen sediment for solid sulfur-bearing mineral extraction was immediately transferred to a glass vial containing enough of 5% zinc acetate solution to submerge the sample. Zero-valent sulfur (ZVS, mainly elemental sulfur) in this study is defined as the sulfur extracted with a methanol/toluene mixture from sediment samples and measured as S_8 by reversed-phase HPLC. This ZVS was extracted from defrosted sediment samples via sustained agitation on a rotary shaker for ~15 hours using a 3:1 methanol:toluene mixture. The sample-to-extractant ratio was ~1/20 (wet weight/volume). The ZVS concentration of the supernatant was quantified via reversed-phase high-performance liquid chromatography (HPLC) using a C-18 column and 98% methanol, 2% water as the eluent (Findlay et al., 2014). The pump speed was set to 1 mL/minute, the detection was conducted at 230 nm with UV detection. Standard curves were made using orthorhombic S_8 dissolved in toluene and encompassed the range of concentrations observed in samples. The detection limit for this method is about

0.5 µM. Polysulfide decomposes to zinc sulfide and elemental sulfur shortly after the sediment is fixed with zinc acetate, thus the contents and isotopic compositions of ZVS reflect the sulfur from both elemental sulfur and polysulfide (Zopfi et al., 2004).

The supernatant and residue were transferred separately to a hot distillation column. The supernatant was extracted with a chromium(II) chloride solution in order to convert ZVS to sulfide. The separated solid residue was treated with a standard two-step sulfide extraction (Fossing and Jørgensen, 1989), extracted with 6N HCl to release the acid volatile sulfur (AVS, mainly Fe monosulfide) and then with a chromium(II) chloride solution to release the chromium reducible sulfur (CRS, mainly pyrite). These three solid-phase sulfur species were recovered in a 5% zinc acetate trap. The contents of AVS and CRS were analyzed after dilution spectrophotometrically at 672 nm by the methylene blue method (Cline, 1969). Sulfide from ZVS, AVS and CRS were converted to silver sulfide by the addition of a silver nitrate solution. The cleaned and dried precipitates then were prepared for sulfur isotope analysis.

Iron sequential extractions were performed at AWI after Poulton and Canfield (2005) (PC method) and Henkel et al. (2016) using ~50 mg of dry sediment and 5 mL of (a) Na-acetate for Fe-carbonates and surface-reduced Fe(II) (Fe_{aca}), (b) hydroxylamine-HCl for easily reducible Fe-oxides (ferrihydrite, lepidocrocite) (Fe_{hyam}), (c) Na-dithionite/citrate for reducible Fe-oxides (mostly goethite and hematite and some magnetite) ($Fe_{di\text{-}ct}$), and (d) ammonium oxalate/oxalic acid for magnetite (Fe_{oxa}). The concentration of iron released from each of the four leachates above was determined by inductively coupled plasma-optical emission spectrometry (ICP-OES; iCAP 7400, Thermo Fisher Scientific). Since AVS is quantitatively extracted by the acetate extractions (step a), the Fe_{aca} content of sediments is reported as the difference between the acetate and AVS extractions (Poulton and Canfield, 2005). Fe_{py} is calculated from the measured pyrite sulfur (CRS) content of each sample assuming 1:2 Fe:S stoichiometry.

A recent study found that Na-acetate extracted substantial amounts of Fe(III) (e.g., amorphous Fe(III)-oxides and ferrihydrite; Laufer et al., 2020). Thus, Fe_{aca} and Fe_{hyam} are composed of Fe-carbonates and poorly crystalline Fe(III) minerals, while $Fe_{di\text{-}ct}$ and Fe_{oxa} include highly crystalline Fe(III) oxides (e.g.,

hematite or goethite) and mixed-valence Fe minerals (e.g., magnetite) (Poulton and Canfield, 2005). Different Fe(III)-containing minerals have different half-lives for the sulfide-promoted reductive dissolution of Fe-(oxyhydr)oxides (Canfield et al., 1992; Poulton et al., 2004). To better distinguish the relative fractions of poorly/highly crystalline Fe(III) minerals, we therefore quantified non-sulfur-bound reactive iron in two different ways: 1) the sum of Fe_{aca} and Fe_{hyam}, 2) PC method: the sum of Fe_{aca}, Fe_{hyam}, $Fe_{di\text{-}ct}$ and Fe_{oxa}. The highly reactive iron (Fe_{HR}) is defined as the sum of Fe_{aca}, Fe_{hyam}, $Fe_{di\text{-}ct}$, Fe_{oxa}, Fe_{AVS} and Fe_{py}, and the extent of pyritization of the highly reactive iron pool is defined as the ratio of Fe_{py} and Fe_{HR} contents (i.e., Fe_{py}/Fe_{HR}). Similarly, the degree of sulfidization (DOS) is defined as the ratio of $Fe_{(py+AVS)}$ and Fe_{HR} contents (i.e. DOS = $Fe_{(py+AVS)}$ / Fe_{HR}). Replicate analysis of standards for the four extractions displayed an average relative standard deviation (RSD) of better than 6%. All solid-phase sulfur and iron data are expressed relative to the wet mass of the sample.

For total organic carbon (TOC) content analysis, dry sediment was decarbonated with H_2SO_3 and determined in a CN analyzer (Carlo Erba NA-1500) by combustion (Beulig et al., 2018). Contents are reported in dry weight percent (wt %) with an RSD of ~2%. Density was measured from wet weight and volume of sediment and expressed as the wet weight per cm^3. Porosity was measured from the volume of sediment and water weight loss after drying at 60 °C until a constant weight was reached (Beulig et al., 2018). Porewater sulfate and methane concentration, porosity and total organic carbon content were previously published (Beulig et al., 2018).

2.4. Stable sulfur isotope analyses

For sulfur isotope analysis of porewater sulfate and sulfide, pore fluid was collected separately, fixed with a saturated barium chloride solution and a 5% zinc acetate solution respectively, and frozen at −20 °C. Porewater sulfate was precipitated as barium sulfate (barite) and zinc sulfide precipitated from porewater sulfide was converted to silver sulfide as above. The cleaned and dried barite and silver sulfide were

combusted at 1030°C in a Flash Element Analyzer (EA), and the resulting sulfur dioxide (SO_2) was measured by continuous helium flow on a gas-source isotope ratio mass spectrometer (GS-IRMS; Thermo Finnegan Delta V Plus) at the Godwin Laboratory, University of Cambridge. We performed similar measurements for porewater sulfate using sulfur monoxide (SO) on a GS-IRMS (Sercon 20-22) at Aarhus University. The isotopic data show good consistency on both IRMS's ($\delta^{34}S_{Cambridge} = 0.998\ \delta^{34}S_{Aarhus} - 0.088$; $R^2 = 0.994$, n = 71). The uncertainty on $\delta^{34}S$ was determined using the standard deviation of the standard NBS 127 at the beginning and the end of each run (~0.3‰, 1σ). Measurements of $\delta^{34}S$ were corrected to NBS 127, IAEA-standards and in-house silver sulfide standards. The $\delta^{34}S$ values are reported with respect to Vienna Canyon Diablo Troilite (V-CDT).

2.5. Diagenetic modeling for the sulfur isotopic composition of pyrite

A diagenetic model is developed to simulate the sulfur isotopic composition of pyrite in the Bornholm Basin sediments. The model is predicated on our observation that most of the sedimentary pyrite rapidly formed near the sediment–water interface, then grew in content slowly over the uppermost 100 cm of the sediment column where porosity is relatively high and constant (e.g., 0.88–0.92 at BB01). Thus, a constant bulk weight-specific rate of pyrite formation below the sediment–water interface was estimated by linear regression of the CRS content versus depth. The total accumulation rate of pyrite during sediment burial was calculated by multiplying this gradient by the sedimentation rate. We assume that the deposition of sediments in the uppermost 100 cm is in steady state since the sedimentation rate is relatively constant (Beulig et al., 2018). The upper sediments were divided into 1 cm intervals starting at the sediment–water interface. Pyrite at a certain depth (depth = i) has an isotopic composition determined by the $\delta^{34}S$ of the overlying original pyrite (depth = $i-1$) plus the newly-formed pyrite at depth i (eq. 1). The $\delta^{34}S$ of the additional pyrite is calculated for both the H_2S pathway and the polysulfide pathway. Butler et al. (2004) proposed that via the H_2S pathway, pyrite has a $\delta^{34}S$ that is a mixture of the $\delta^{34}S$ of the Fe monosulfide and the $\delta^{34}S$ of the H_2S (eq. 2), while via the polysulfide pathway the pyrite inherits a $\delta^{34}S$ dominated by the

$\delta^{34}S$ of the polysulfide (eq. 3). Consequently, we suggest the following equations to model the $\delta^{34}S$ of pyrite in the near-surface sediment column (i.e., 0–100 cmbsf):

$$m_i F^{3X}S_i = m_{i-1} F^{3X}S_{i-1} + m_{new} F^{3X}S_{new} \quad (1)$$

$$F^{3X}S_{new} = (F^{3X}S_{H2S} + F^{3X}S_{FeS})/2 \quad (FeS + H_2S \rightarrow FeS_2 + H_2) \quad (2)$$

$$F^{3X}S_{new} = F^{3X}S_{polysulfide} \quad (FeS + S_x^{2-} \rightarrow FeS_2 + S_{x-1}^{2-}) \quad (3)$$

where the *m* represents the molar quantity of pyrite in each depth interval *i* and the *F* represents fractional isotopic abundances of ^{32}S or ^{34}S (i.e., 3X = 32 or 34). The above equations can be written in approximate form by replacing the $F^{3X}S$ with $\delta^{34}S$. The $\delta^{34}S$ of H_2S, FeS and polysulfide at each depth are calculated based on linear interpolations from depths with measured $\delta^{34}S$ values. Combining equation 1 with equation 2 or 3, the modeled $\delta^{34}S$ of pyrite can be calculated. In the model, we assume that the $\delta^{34}S$ of AVS and ZVS reflects the $\delta^{34}S$ of solid-phase Fe monosulfide and polysulfide, respectively. In reality, however, ZVS includes both polysulfide and elemental sulfur. The $\delta^{34}S$ of polysulfide could be higher than the assumed values due to the surficial, but not complete, isotope exchange between elemental sulfur and aqueous sulfide (see section 4.2; Fossing and Jørgensen, 1990; Fossing et al., 1992). Therefore, our results for modeling the polysulfide pathway and the H_2S pathway should be considered as the hypothetical minimum and maximum $\delta^{34}S$ values of pyrite, respectively, which may not be used to quantify the contribution of each pathway to the bulk pool of pyrite. Additionally, since the $\delta^{34}S$ of AVS and ZVS is only measured in the top centimeters at site BB05, we assume that their values in deeper sediments largely resemble those in neighboring cores (cf. BB01). Using different $\delta^{34}S$ input values for AVS and ZVS (e.g., measured data at BB01 and BB02) makes a difference of up to 2.7‰ in the modeling result of BB05.

3. RESULTS

3.1. Sediment stratigraphy

The sediments of the Bornholm Basin show a distinct stratigraphy due to changes in the depositional environment since the last glacial period (Andrén et al., 2000; Sohlenius et al., 2001; Jensen et al., 2017). According to seismo-acoustic mapping and lithological analysis, glacial tills were deposited on the bedrock during the last glacial period and overlain by lacustrine clay from the Baltic Ice Lake (Moros et al., 2002; Jensen et al., 2017). The clay deposited from the brackish Yoldia Sea and the lacustrine Ancylus Lake covered this ice lake clay before 8.5 ka BP (Moros et al., 2002; Jensen et al., 2017). Those clay deposits in the Bornholm Basin were characterized by low organic carbon content, as seen in the bottom of sites BB02 and BB05 (Figs. 3C and 4C). As sea level rose after the last glacial period, the continuous inflow of seawater into the Baltic Sea coupled with the warmer climates resulted in a general increase in primary productivity and subsequent increase in sedimentary organic carbon content (Andrén et al., 2000; Sohlenius et al., 2001) (Figs. 2C, 3C and 4C). The inflow of seawater also induced stratification of the water column, enhancing the preservation of organic matter at the seafloor. This lithological boundary marks the transition from lacustrine clay to the Littorina Sea mud deposit termed the Holocene Mud Layer (HML; Hilligsøe et al., 2018). At sites BB02 and BB05, the TOC contents were ca. 0.6 wt % in the lacustrine clay deposits and ca. 4–6 wt % in the HML (Figs. 3C and 4C). The high TOC content throughout core BB01 indicates that the marine–lacustrine transition is below the bottom of the core (Fig. 2C). The thickness of the HML is controlled by major faults in the basin where the thickest HML is found near the fault scarp to the southwest of the basin (Jensen and Endler, 2012; Jensen et al., 2017). The collected sediments have a grey color in Holocene marine mud and a light-brown color in the lacustrine clay. Distinct black bands are found at ca. 360–480 cmbsf at site BB02 and ca. 350–520 cmbsf at site BB05. These black bands represent the modern depth of the sulfidization front (as determined by subsequent chemical analyses). The sedimentation rate of the HML was nearly constant over 8.5 ka at each site according to ^{14}C dates of shells and seismo-acoustic

markers (Beulig et al., 2018). The sedimentation rates at BB01, BB02 and BB05 were 0.065, 0.053, 0.049 cm y^{-1}, respectively (Table 1).

3.2. Porewater geochemistry

Panels A–C in Figures 2–4 present the porewater profiles of sulfate, methane, aqueous sulfide, dissolved ferrous iron and dissolved barium at sites BB01, BB02 and BB05. Sites BB01/02 and BB05 represent two different types of sulfate and methane pore-fluid profiles in the Bornholm Basin. Sulfate concentrations decrease downward from the sediment surface and are depleted at 0.6 mbsf, 0.7 mbsf and 3.7 mbsf at sites BB01, BB02 and BB05, respectively. Steep gradients of sulfate and methane at sites BB01 and BB02 define sharp sulfate–methane transitions (SMT) at 0.6 mbsf and 0.7 mbsf, respectively (Figs. 2A and 3A). Methane concentrations reach a maximum of up to 1.4 mM in the middle of Holocene marine mud and drop to 35 μM in the lacustrine clay at site BB02 (Fig. 3A). In the periphery of the Basin, no accumulation of methane (<13 μM) is observed in the 7-m-long core BB05, whereas porewater sulfate concentrations reach a minimum of ca. 2 μM at 367 cmbsf (Fig. 4A). The lacustrine clay at sites BB02 and BB05 contains a small relic sulfate pool from which sulfate diffuses upwards (Figs. 3A and 4A).

The concentrations of aqueous sulfide are near zero (<3 μM) in the uppermost centimeters and increase steeply with depth, reaching peaks of 2.0–3.1 mM at around 60 cmbsf at sites BB01, BB02 and BB05 (Figs. 2B, 3B and 4B). The concentrations of aqueous sulfide drop gradually below the peak and reach zero at ca. 400 cmbsf where the aqueous sulfide meets dissolved ferrous iron at both BB02 and BB05. Dissolved ferrous iron concentrations are near zero (<7 μM) above ~400 cmbsf with a few exceptions close to the sediment–water interface, whereas it starts to accumulate in the lacustrine clay, reaching ~0.2 mM at the bottom of cores BB02 and BB05. Dissolved barium concentrations increase with depth and peak at ~400 cmbsf, and then decrease from ~13 μM to 2 μM between 400–700 cmbsf at sites BB02 and BB05 (Figs. 3C and 4C).

3.3. Solid-phase sediment geochemistry

Panels D–F in Figures 2–4 present the solid-phase sediment profiles of sulfur and iron at sites BB01, BB02 and BB05. The three sites show similar patterns of zonation in solid-phase sulfur and iron geochemistry. The AVS and ZVS contents drop steeply with depth from ca. 10 μmol g^{-1} near the sediment surface to low values, <1 μmol g^{-1}, below ca. 100 cmbsf at the three sites (Figs. 2E, 3E and 4E). The AVS and ZVS contents remain low throughout the rest of the cores with the exceptions of sharp peaks at ca. 400–500 cmbsf (Figs. 3E and 4E), which are visible as distinct black bands at sites BB02 and BB05.

The main sulfur pool in Holocene marine sediments is CRS. AVS and ZVS concentrations are generally one or two orders of magnitude lower than those of CRS in Holocene marine mud. The content of CRS increases with depth in the uppermost 100 cm at the three sites, ranging from 26 μmol g^{-1} to 196 μmol g^{-1} (Figs. 2F, 3F and 4F). The content of CRS stays constant at ca. 200 μmol g^{-1} below 100 cmbsf until the marine–lacustrine transition at BB02 and BB05. Below the sulfidization front at ca. 400–500 cmbsf, CRS contents are very low, down to 0.64 μmol g^{-1} (Figs. 3F and 4F).

Contents of non-sulfur-bound reactive Fe (four extractions by the PC method) display an opposite trend to those of CRS (Figs. 2D, 3D and 4D). Generally, contents of non-sulfur-bound reactive Fe in the lacustrine clay are three or four times higher than those in Holocene marine mud (Figs. 3D and 4D). The content of non-sulfur-bound reactive Fe peaks at ca. 10–25 cmbsf and decreases with depth in the uppermost 100 cm. Its content stays constant at ca. 10–20 μmol g^{-1} in the deeper Holocene marine sediments, with contents ranging from 40 μmol g^{-1} to 78 μmol g^{-1} below ca. 400 cmbsf at BB02 and BB05.

The Fe_{py}/Fe_{HR} near the sediment–water interface ranges from 0.3 to 0.6 and increases with depth in the uppermost 100 cm, remaining at a constant level of around 0.9 between 100 and 400 cmbsf (Figs. 2F, 3F and 4F). The Fe_{py}/Fe_{HR} in the lacustrine clay is lower than 0.1 at BB02 and BB05. The values of Fe_{py}/Fe_{HR}

and DOS are very similar since Fe monosulfide is a minor fraction through the cores. Where applicable, the Fe_{py}/Fe_{HR} values are used to compare our results to those reported in the literature (cf. Fig. 5).

3.4. Sulfur Isotopes

Panels G–H in Figures 2–4 show the sulfur isotopic compositions of dissolved and solid-phase sulfur species at sites BB01, BB02 and BB05. The $\delta^{34}S$ of bottom water sulfate is 21‰. The $\delta^{34}S$ of porewater sulfate increases steeply with depth below the sediment–water interface with near-linear or converging profiles in Holocene marine sediments of the three sites. Similarly, the $\delta^{34}S$ of porewater sulfide increases with depth from ca. −30‰ to ca. 21‰ at the three sites, forming a plateau that extends to the base of Holocene marine mud where aqueous sulfide concentrations drop to zero. Below the marine–lacustrine transition, the $\delta^{34}S$ of sulfate decreases with depth at both sites BB02 and BB05.

The $\delta^{34}S$ values of AVS and ZVS are close to each other at the same depth among the three sites, ranging from ca. −30‰ to ca. −20‰ in the uppermost 60 cm sediments. At BB02, the $\delta^{34}S$ of both AVS and ZVS, however, increases with depth from −21‰ to −8‰ between 60 cmbsf and 99 cmbsf (Fig. 3G). The $\delta^{34}S$ of AVS and ZVS at ca. 400–500 cmbsf is higher than that in the surface at BB02 and BB05, ranging from 4‰ to 31‰ (Figs. 3G and 4G). The $\delta^{34}S$ of CRS is rather invariant in the upper sediment column at each of the three sites, with averages of −22‰ ± 5‰, −32‰ ± 4‰ and −37‰ ± 3‰ (1σ) at BB01, BB02 and BB05, respectively (Figs. 2G, 3G and 4G). The $\delta^{34}S$ of CRS increases with depth between ca. 300 cmbsf and ca. 460 cmbsf at BB02 and BB05. Interestingly, the contents and the $\delta^{34}S$ of CRS display a negative correlation in the lacustrine clay at sites BB02 and BB05 (Fig. 6).

4. DISCUSSION

4.1. Pyrite accumulation with depth in near-surface sediments

The deep Bornholm Basin is generally hypoxic with seasonal anoxia, with the exception of periodic inflows of saline and oxygenated bottom water originating from the North Sea (Boesen and Postma, 1988; Carstensen et al., 2014). Macrobenthos are rare and bioturbation is not well developed but does occur after periods of oxic seawater inflow (Andrén et al., 2015). The bottom water in the Bornholm Basin has been non-sulfidic since the onset of marine deposition (perhaps except for a limited period at 8 ka BP; Fonselius, 1981; Conley et al., 2009; Dijkstra et al., 2018), suggesting that Fe sulfide minerals are only formed in the sediment. Rapid pyrite formation appears to occur close to the sediment–water interface, where CRS contents range from 26 to 62 μmol g^{-1} at 0–3 cmbsf (BB01, BB02 and BB05). Despite the low concentration of aqueous sulfide at the sediment–water interface, sulfide oxidation occurs most intensively near the sediment–water interface of the Bornholm Basin (Findlay et al., 2020) due to the high rates of sulfate reduction (Beulig et al., 2018) and the high availability of oxidants (Thamdrup et al., 1994), such as nitrate, Mn-oxides and Fe-oxides. Among these oxidants, non-sulfur-bound reactive Fe(III) (hereafter termed reactive Fe) is suggested to dominate sulfide oxidation near the sediment–water interface (Canfield, 1989; Canfield et al., 1992; Thamdrup et al., 1994; Findlay et al., 2020). The reaction between reactive Fe and aqueous sulfide produces sulfate, elemental sulfur and Fe monosulfide (Zopfi et al., 2008; Holmkvist et al., 2011; Findlay et al., 2020), as shown by the distribution of ZVS and AVS which both have peaks near the sediment surface (Figs. 2E, 3E and 4E). The surface aqueous sulfide pool is replenished by a flux of aqueous sulfide diffusing up from below (e.g., Jørgensen et al., 2004), which is effectively oxidized or trapped as solid-phase sulfur without reaching the overlying water column. In addition, both cable bacteria and sulfur-oxidizing bacteria (*Beggiatoaceae*) were found in the studied area, accelerating microbial sulfide oxidation via metabolic activity in the surface sediment (Hermans et al., 2019). Consequently, intensive sulfide oxidation coupled to Fe reduction and subsequent formation of Fe monosulfide and elemental sulfur promote rapid pyrite formation close to the sediment–water interface.

Progressive pyrite accumulation with depth has been observed within marine sediments (Jørgensen, 1978; Canfield et al., 1992; Zopfi et al., 2008; Holmkvist et al., 2011; Lin et al., 2016). In the Bornholm Basin, CRS contents similarly increase with depth below the sediment–water interface (Figs. 2F, 3F and 4F). Data from cores BB02 and BB05 are good examples. The content of CRS reaches a maximum at ca.100 cmbsf, before staying constant at ca. 200 μmol g^{-1}. High AVS content coexists with high ZVS content in the uppermost sediments (Figs. 2E, 3E and 4E). The content of ZVS and AVS decreases with depth to low background values through the uppermost 100 cm, concurrent with an increase in CRS content, which is the dominant end product. Elemental sulfur and Fe monosulfide, therefore, are the most likely precursors for pyrite formation in the uppermost 100 cm as has been demonstrated by previous studies (e.g., Rickard and Morse, 2005; Holmkvist et al., 2014). Besides the transformation of Fe monosulfide to pyrite, pyrite accumulation is also corroborated by the Fe record. Content of reactive Fe broadly decreases with depth at 20–100 cmbsf and stays constant in the deeper Holocene marine sediments (Figs. 2D, 3D and 4D). The degree of sulfidization (DOS = $Fe_{(py+AVS)}$ / Fe_{HR}) increases from 0.3–0.6 near the sediment–water interface to 0.9 at 100 cmbsf, indicating a gradual transformation with depth of reactive Fe to Fe sulfide minerals (Böttcher and Lepland, 2000), which are ultimately preserved as pyrite. Therefore, the diminishing ZVS, AVS and reactive Fe pools contribute to the formation of pyrite with depth in the uppermost 100 cm.

Two factors may ultimately limit pyrite formation in marine sediments: the availability of aqueous sulfide or the availability of reactive Fe (e.g., Berner, 1984; Boesen and Postma, 1988; Middelburg, 1991; Canfield et al., 1992; Kasten et al., 1998; Neretin et al., 2004; Fu et al., 2008; Roberts, 2015; Shawar et al., 2018). From 100 cmbsf to the base of Holocene marine sediments, where the sulfidization front is found, pyrite content reaches ca. 200 μmol g^{-1} and the DOS stays constant at 0.9. Here, the reaction between aqueous sulfide and reactive Fe appears to have largely stopped, though aqueous sulfide is available. In marine settings with high organic carbon content (e.g., the Baltic and Black Seas), organoclastic sulfate reduction and sulfate reduction coupled to anaerobic oxidation of methane (AOM) produce high concentrations of aqueous sulfide, which consumes most of the reactive Fe phases (Neretin et al., 2004; Holmkvist et al.,

2011, 2014). Consequently, the stable DOS and the high concentration of aqueous sulfide at 100–400 cmbsf suggest that the amount of Fe that becomes sulfidized is limited by the availability of reactive Fe in Holocene marine sediments. By contrast, in the lowermost part of the sediment column at sites BB02 and BB05, high contents of reactive Fe are found coinciding with the lowest DOS and aqueous sulfide below detection limit. Thus, we conclude that pyritization is limited by the availability of aqueous sulfide in the deeper lacustrine sediments.

We note that a small amount of non-sulfur-bound "reactive Fe" remains at depth even though there is sulfide present at 100–400 cmbsf. It is possible that the current Fe extraction technique developed by Poulton and Canfield (2005) does not discriminate completely between highly-reactive Fe and much less reactive sheet-silicate-Fe. For example, hydroxylamine-HCl and Na-dithionite/citrate solutions extract a small amount of Fe from certain sheet silicate minerals (Chester and Hughes, 1967; Raiswell et al., 1994). A recent study also showed that the majority of Fe in the ammonium oxalate/oxalic acid extraction is not dissolved from magnetite, but instead comes from Fe-bearing clays (Slotznick et al., 2020). Therefore, the broad depletion of non-sulfur-bound reactive Fe seen at 100–400 cmbsf may indicate the exhaustion of readily pyritizable Fe on the time scales of deposition in the Bornholm Basin.

The Fe_{py}/Fe_{HR} (which was initially termed the degree of pyritization) has been widely used as a proxy to reconstruct environmental conditions of deposition throughout Earth's history (Raiswell et al., 1988, 2018; Lyons et al., 2009; Li et al., 2010; Raiswell and Canfield, 2012). It is suggested that the Fe_{py}/Fe_{HR} can be used to distinguish between deposition in anoxic, non-sulfidic or sulfidic conditions in the bottom water when sediments show evidence of anoxic deposition (Canfield et al., 1996; Raiswell and Canfield, 1998; Anderson and Raiswell, 2004; Lyons and Severmann, 2006; Poulton and Canfield, 2011). For example, observations in modern sediments and ancient sedimentary successions suggest that an Fe_{py}/Fe_{HR} of 0.7–0.8 characterizes an upper limit for anoxic non-sulfidic deposition (e.g., März et al., 2008a; Poulton and Canfield, 2011). However, sedimentary sulfide minerals may result from and thus carry an overprint from later diagenetic processes, and thus the Fe_{py}/Fe_{HR} may not reflect geochemical and redox conditions at the

sediment–water interface (e.g., Jørgensen et al., 2004; Riedinger et al., 2017; Hardisty et al., 2018). In the Bornholm Basin, the DOS values are slightly higher than Fe_{py}/Fe_{HR} near the sediment surface but almost equal to Fe_{py}/Fe_{HR} below, since Fe monosulfide becomes a trace component of the Fe pool with depth. From the preceding discussion, we suggest that the increase of Fe_{py}/Fe_{HR} with depth and the extremely high subsurface Fe_{py}/Fe_{HR} of up to 0.93 reflect subsurface diagenetic pyrite accumulation. In general, the deep Bornholm Basin has been hypoxic with seasonal anoxic but non-sulfidic bottom water since the onset of marine deposition (Carstensen et al., 2014), whereas our measured Fe_{py}/Fe_{HR} ratios substantially exceed the upper limit for anoxic non-sulfidic deposition (i.e. 0.7–0.8). Consequently, although the Fe_{py}/Fe_{HR} values of sediments should be high in a euxinic environment (anoxic and sulfidic), exceptions do exist (e.g., Hardisty et al., 2018), and its use as a proxy for past bottom water euxinia needs to be supported by other independent indicators in sedimentary records (e.g., trace elements; Lyons et al., 2009; Rickard, 2012a; Algeo and Li, 2020; Bennett and Canfield, 2020).

Along with Fe_{py}/Fe_{HR}, Fe_{HR}/Fe_T is another widely used iron-speciation parameter in sedimentary rocks, which allows oxic ($Fe_{HR}/Fe_T \leq 0.22$) and anoxic ($Fe_{HR}/Fe_T \geq 0.38$) depositional conditions to be distinguished (Raiswell and Canfield, 1998, 2012; Poulton and Raiswell, 2002; Anderson and Raiswell, 2004; Li et al., 2010; Poulton and Canfield, 2011; Raiswell et al., 2018). Intermediate Fe_{HR}/Fe_T values (0.22–0.38) may still indicate anoxic environments ("possibly anoxic"), but this needs to be supported by other evidence (Poulton and Canfield, 2011; Raiswell et al., 2018). The total Fe abundance (864 ± 45 μmol g^{-1}; 1σ, on a dry weight basis) in a neighboring core (IODP M0065; Dijkstra et al., 2018) suggests that the total Fe deposited in the Bornholm Basin is broadly constant without stratigraphic variation in Holocene marine sediments, allowing us to estimate the Fe_{HR}/Fe_T, albeit with caveats. We calculate an average Fe_{HR}/Fe_T value of about 0.39 (± 0.08; 1σ) in the marine sediments of sites BB01, BB02 and BB05. These results are close to the expected boundary value between "possibly anoxic" and "anoxic" deposition (i.e., 0.38; e.g., Poulton and Canfield, 2011), which is only partly consistent with the hypoxic environment in the deep Bornholm Basin (Carstensen et al., 2014). Generally, iron-speciation data with $Fe_{HR}/Fe_T \geq 0.38$ and

$Fe_{py}/Fe_{HR} \geq 0.8$, such as the sediments in the Bornholm Basin (Fig. 5), previously have been suggested to indicate euxinic depositional conditions (e.g., Li et al., 2010; Poulton and Canfield, 2011; Raiswell et al., 2018). This contradicts the known bottom water conditions. Although the Bornholm Basin may not be representative of open marine settings, extra caution is warranted when using iron-speciation data that are close to the boundary values to reconstruct past water-column chemistry.

4.2. Sulfur isotopic differences between solid-phase sulfur and aqueous sulfide

The sulfur isotopic composition ($\delta^{34}S$) of aqueous sulfide is close to that of AVS and ZVS in the uppermost 10 cm. Such a similarity confirms that Fe monosulfide and elemental sulfur are formed without significant sulfur isotopic fractionation (Fry et al., 1986), through the reaction between reactive Fe and aqueous sulfide. Sulfate reduction coupled to AOM consumes downward-diffusing sulfate in the sediment, preferentially removing ^{32}S and enriching ^{34}S in the residual porewater sulfate and in the subsequently produced aqueous sulfide (e.g., Canfield, 2001; Turchyn et al., 2016; Jørgensen et al., 2019). This sulfur isotope fractionation, combined with the independent diffusion of ^{32}S and ^{34}S in sulfate and sulfide, causes the aqueous sulfide pool around the SMT to approach the $\delta^{34}S$ of seawater sulfate (Jørgensen, 1979; Jørgensen et al., 2004). While porewater sulfide $\delta^{34}S$ increases parallel to that of porewater sulfate, sulfur isotopic differences are observed between porewater sulfide and AVS/ZVS in the subsurface sediments at BB01 and BB02. Laboratory radiotracer experiments found that sulfur isotope exchange between ^{35}S-labeled aqueous sulfide, polysulfide, elemental sulfur and Fe monosulfide reaches equilibrium within hours (Fossing and Jørgensen, 1990; Fossing et al., 1992). However, this equilibrium does not mean that isotopic ratios are the same in the different sulfur species. It only means that the forward and backward fluxes of isotopes among the sulfur pools reached parity.

The shrinking pools of AVS and ZVS are exposed to a large pool of aqueous sulfide in the subsurface sediments (e.g., 50–100 cmbsf). Although porewater sulfide $\delta^{34}S$ approaches +21‰ below 50 cmbsf, the

$\delta^{34}S$ of AVS and ZVS remains invariant (ca. −30‰ to −20‰) throughout core BB01. If assuming a complete sulfur isotope exchange among the reduced sulfur species, the $\delta^{34}S$ of AVS and ZVS, however, should be close to +21‰ since the isotopic fractionation between sulfide and elemental sulfur is typically small (e.g., < 5‰; Fry et al., 1986). Therefore, the large isotopic differences of up to 43‰ indicate that the bulk pools of AVS and ZVS do not freely undergo sulfur isotope exchange with porewater sulfide. It is possible that the equilibrium between elemental sulfur and sulfide, which proceeds through polysulfide species, depends upon the form of elemental sulfur (Kamyshny and Ferdelman, 2010). There might be a quasi-equilibrium reached with dissolved sulfur species and the surface sulfur atoms of the solid-phase species, but the bulk sulfur isotopic composition of solid-phase species remains unchanged. Scanning electron microscopy reveals that crystalline elemental sulfur aggregates in marine sediments feature a quasi-concentric structure, with a higher abundance of sulfur in their core relative to their rim (Lin et al., 2015; Liu et al., 2020). Therefore, we suggest that an active isotope exchange occurs between aqueous sulfide and the rim of elemental sulfur (e.g., Fossing et al., 1992), whereas the core of the elemental sulfur granules is less likely to be involved in isotope exchange and retains its original isotopic signature. Consequently, we conclude that most of the ZVS in Holocene marine sediments is formed via intensive oxidation of aqueous sulfide close to the sediment surface. The bulk of the ZVS has a $\delta^{34}S$ signature close to that of aqueous sulfide in the surface centimeters of the sediments and we propose is subject to only minor sulfur isotope exchange during burial into the deeper subsurface where it acts as a significant intermediate for pyrite formation.

The $\delta^{34}S$ of pyrite depends on primarily the relative depth within the sulfate–sulfide gradients it forms ("relative depth" defined by the fraction of sulfate remaining) (Jørgensen et al., 2004). Near the sediment–water interface, the isotopic similarity among all sulfur species suggests that the $\delta^{34}S$ of pyrite, Fe monosulfide and elemental sulfur is inherited from aqueous sulfide, and pyrite is rapidly formed at this horizon. Pyrite then accumulates only slowly deeper in the sediment. The ongoing formation of pyrite at depth appears to remain an important sink for both sulfur and reactive Fe down to 100 cmbsf where both

CRS content and Fe_{py}/Fe_{HR} reach a maximum. The deeper the pyrite forms, the more ^{34}S-enriched the porewater sulfate and, therefore, also the aqueous sulfide produced, from which the pyrite precipitates (Jørgensen et al., 2004; Shawar et al., 2018). Interestingly, although porewater sulfide $\delta^{34}S$ increases parallel to that of porewater sulfate, the $\delta^{34}S$ of CRS remains at ca. −30‰ throughout the subsurface sediments. A similar pattern of ^{34}S-enriched aqueous sulfide relative to coexisting pyrite has been widely observed in marine subsurface sediments (e.g., Kaplan et al., 1963; Chanton et al., 1987; Canfield et al., 1992; Formolo and Lyons, 2013; Raven et al., 2016). The interpretation of this sulfur isotopic difference includes isotope exchange with organic-bound sulfur (Raven et al., 2016) and sulfur disproportionation (Habicht and Canfield, 1997, 2001). We will consider both of these for the sediments in the Bornholm Basin.

Raven et al. (2016) proposed that the ambient aqueous sulfide might be enriched in ^{34}S relative to the sulfide produced by sulfate reduction in the vicinity where pyrite precipitates. In marine sediments, the $\delta^{34}S$ of organic-bound sulfur is more positive and less variable than that of pyrite (e.g., Brüchert et al., 1995; Raven et al., 2016; Riedinger et al., 2017; Shawar et al., 2018). Aqueous sulfide and one type of organic-bound sulfur (i.e., proto-kerogen) have similar $\delta^{34}S$ values in the upper sediments of the Santa Barbara Basin, while they are enriched in ^{34}S relative to coeval pyrite (Raven et al., 2016). The discrepancy between pyrite and aqueous sulfide $\delta^{34}S$ was thus interpreted as the result of sulfur isotopic exchange between aqueous sulfide in porewater and organic-bound sulfur, which would tend to enrich the aqueous sulfide pool in ^{34}S (Raven et al., 2016). The exact mechanism of this proposed role of organic sulfur in pyrite $\delta^{34}S$ requires further experimental investigation.

Sulfide oxidation to intermediate valence state sulfur species (e.g., elemental sulfur) and subsequent disproportionation can lead to large sulfur isotope fractionation (Canfield and Thamdrup, 1994; Böttcher et al., 2001; Pellerin et al., 2019). Several studies have shown that the $\delta^{34}S$ of aqueous sulfide directly produced during sulfate reduction in incubated vials are uniformly more positive than those of coexisting pyrite extracted from the sediments (Habicht and Canfield, 1997, 2001). The relatively low $\delta^{34}S$ in pyrite

was suggested to require the combined activity of sulfate-reducing microorganisms with additional sulfur isotope fractionation during the oxidative and disproportionation part of the sulfur cycle (Habicht and Canfield, 2001; Zopfi et al., 2008). In the Bornholm Basin, however, elemental sulfur (ZVS) below the surface has $\delta^{34}S$ matching those of pyrite, not of aqueous sulfide (e.g., BB01), suggesting that the elemental sulfur in subsurface sediments is not a direct oxidative product of aqueous sulfide at depth (e.g., Raven et al., 2016). Consequently, sulfur disproportionation does not appear to be a reason for this sulfur isotopic difference between pyrite and coexisting aqueous sulfide in the Bornholm Basin sediments. It should be noted that the bulk pyrite pool at depth includes some pyrite that initially precipitated at the surface. Thus, it would be useful to develop a more complete diagenetic model to resolve the observed sulfur isotopic difference, which we do in the next section.

4.3. The role of near-surface pyrite formation in the stable sulfur isotopic composition of bulk pyrite

Following the method described in section 2.5, a simple diagenetic model is used to understand the $\delta^{34}S$ of pyrite in the study area and model results are shown in Figs. 2H, 3H and 4H. The model simulates the $\delta^{34}S$ of pyrite very well at BB01 (Fig. 2H). For clarity, we refer to the pyrite formed close to the sediment–water interface (e.g., 0–10 cmbsf) as "original" pyrite and in the subsurface sediments (e.g., 10–100 cmbsf) as "newly-formed" or "additional" pyrite. The additional pyrite formed via the H_2S pathway at depth has an isotopic composition that is a mixture of the $\delta^{34}S$ of Fe monosulfide and H_2S at the depth where it forms, while via the polysulfide pathway it inherits a $\delta^{34}S$ dominated by that of polysulfide (Butler et al., 2004). The newly-formed pyrite is added to the bulk pyrite originating near the surface sediment, which is considerably lower in $\delta^{34}S$ than aqueous sulfide at depth. Our results demonstrate that although pyrite is continuing to form throughout the sediment column, its $\delta^{34}S$ is not as influenced by the isotopically higher pool of aqueous sulfide in the deeper part of the sediment since most of the pyrite accumulates during the early stages of burial (Jørgensen, 1979). It should be noted that many of the pyrite $\delta^{34}S$ values below 30 cmbsf are 1‰–6‰ lower than that in the surface centimeters at BB02 and BB05, suggesting that the original

pyrite formed when this sediment was at the sediment–water interface had an even lower $\delta^{34}S$ value. The model was re-run with slightly lower $\delta^{34}S$ of the initial pyrite at 0–1 cmbsf (i.e., −38‰ at BB02; −46‰ at BB05), which simulates these low $\delta^{34}S$ values very well (Figs. 3H and 4H). These low $\delta^{34}S$ values, in turn, indicate that the bulk $\delta^{34}S$ of aqueous sulfide near the sediment–water interface may vary on a time scale of 100–1000 years. Taken together, our data suggest that the additional pyrite has a minor effect on the $\delta^{34}S$ of the bulk pyrite at depth, which explains why subsurface pyrite has a $\delta^{34}S$ similar to that of pyrite in the surface sediment. This diagenetic process and the associated isotopic pattern are possibly of relevance for marine sediments with high organic matter content, and high aqueous sulfide but low reactive Fe availability.

While two pathways of pyrite formation are modeled for the three sites, their relative importance is unclear. The polysulfide pathway involves the dissolution of Fe monosulfide and subsequent reaction with aqueous polysulfide to form pyrite (Rickard, 1975; Luther, 1991). The H_2S pathway involves the dissolution of Fe monosulfide and reaction with dissolved H_2S, while HS^- does not participate in the reaction (Rickard, 1997; Thiel et al., 2019). The importance of the H_2S pathway, therefore, is pH-dependent and is favored in near neutral to acidic conditions as H_2S becomes the dominant constituent of aqueous sulfide (Butler et al., 2004; Rickard and Luther, 2007). By contrast, the polysulfide pathway is favored at alkaline pH and is controlled by the concentration of aqueous sulfide and elemental sulfur (Kamyshny and Ferdelman, 2010; Holmkvist et al., 2014; Findlay, 2016). Yücel et al. (2010) argued that, provided that elemental sulfur was present to form polysulfide, the polysulfide pathway would dominate pyrite formation, at least for the Black Sea sediments.

With respect to the Bornholm Basin sediments, H_2S is a minor component in the total aqueous sulfide pool due to a relatively high pH of 8 (Andrén et al., 2015), potentially limiting the H_2S pathway in the near-surface sediments. Similarly, the high availability of elemental sulfur (ZVS) and the presence of aqueous sulfide in the uppermost 100 cm may provide favorable conditions for polysulfide formation and subsequent pyrite formation via the polysulfide pathway. In deeper sediments, the importance of the H_2S pathway

increases over the polysulfide pathway due to much higher aqueous sulfide concentrations. Due to the nearly complete exhaustion of the reactive Fe pool, however, pyrite is not formed in the deeper Holocene marine sediments, as seen in the CRS contents that stay constant and reach a plateau of around 200 μmol g^{-1}. This suggests that solid-phase sulfide formation is a negligible sink for aqueous sulfide in the porewater over this interval. The exception for the deeper sediments is the sulfidization front where the formation of ZVS and AVS is currently occurring. Thus, the polysulfide pathway may become important for pyrite formation at depth since the sulfidization front is the main sink for downward diffusing sulfide (Jørgensen et al., 2004; Neretin et al., 2004; Holmkvist et al., 2014; Riedinger et al., 2017). Recently, a novel ferric-hydroxide-surface (FHS) pathway for pyrite formation was proposed, in which surface-complexed $>Fe^{II}OH_2^+$ reacts with sulfide to form an attached $>Fe^{II}S_2^-$ precursor to pyrite (Peiffer et al., 2015; Wan et al., 2017). This reaction mechanism was hypothesized to be particularly important when Fe(III) concentration is in excess of aqueous sulfide (Wan et al., 2017). We suggest that this new pathway, the FHS pathway, may be important in the deep Fe(III)-rich lacustrine sediments of the Bornholm Basin. The quantitative importance of each pathway, however, remains an open question and future efforts should focus on experimental investigation to develop a more reliable master equation for the rate of pyrite formation via different mechanisms in marine sediments (e.g., Rickard and Luther, 2007).

4.4. Pyrite formation at and below the sulfidization front

In the sediments of the Baltic and Black Seas, aqueous sulfide diffuses from Holocene marine mud into underlying lacustrine clay where it reacts with solid-phase reactive Fe(III) and dissolved ferrous Fe, which diffuses up from below (Jørgensen et al., 2004; Neretin et al., 2004; Holmkvist et al., 2014). In the deep lacustrine clay, a sulfidization front (S-front) is therefore formed by the progressing downward sulfidization of reactive Fe to pyrite (e.g., Neretin et al., 2004; Holmkvist et al., 2014). In the Bornholm Basin, two of our cores at sites BB02 and BB05 cover the entire Holocene marine sediment column and reach the S-front at the fresh-brackish water transition (ca. 4.5 mbsf at BB02; ca. 4.2 mbsf at BB05) where TOC contents

drop to a minimum of 0.6%. The S-fronts are marked by a black band of amorphous Fe sulfide with peaks in AVS and ZVS and with strong opposite gradients in the contents of CRS and reactive Fe.

Such reaction fronts are widespread in other areas of the Baltic Sea and the Black Sea, however, their locations within the sediment column vary from site to site (e.g., Jørgensen et al., 2004; Holmkvist et al., 2011, 2014). In the Black Sea sediments, the S-fronts are generally found in lacustrine clay sediments, largely below the fresh–brackish water transition (Calvert et al., 1996; Jørgensen et al., 2004; Neretin et al., 2004). In contrast, in the Baltic Sea sediments, the S-fronts are located at or right below the fresh–brackish water transition (Boesen and Postma, 1988; Sternbeck and Sohlenius, 1997; Böttcher and Lepland, 2000; Holmkvist et al., 2011, 2014). In the Black Sea, aqueous sulfide is produced in both marine and lacustrine depositions as the SMT penetrates into the lacustrine sediments. This may be due to lower sedimentation rates and higher bottom-water sulfide concentrations in the deep basin of the Black Sea compared to the Bornholm Basin (Dijkstra et al., 2018). In contrast, higher sedimentation rates mean that the depth of sulfate penetration, and thus the maximum depth of aqueous sulfide formation, move faster upwards and away from the lacustrine deposit over time, which gradually dampens the flux of aqueous sulfide to the S-front and slows down the sulfidization rate of the solid-phase Fe minerals. In addition, higher sedimentation rates lead to a more efficient burial of reactive Fe-oxide minerals (e.g., Hensen et al., 2003; Riedinger et al., 2005, 2014, 2017; März et al., 2008b; Oni et al., 2015), which are then available for higher rates of Fe reduction in the lower lacustrine sediments and higher upward fluxes of dissolved ferrous Fe into the S-front. This combined effect of higher sedimentation rates causes a relatively shallow location of the S-front in the sediments of the Bornholm Basin compared to those of the Black Sea. Consequently, we conclude that the location of the S-fronts is controlled by the downward flux of aqueous sulfide from the SMT, as well as the rate of Fe reduction in the lacustrine sediments and the resulting upward flux of dissolved ferrous Fe.

The sulfur isotopic composition of CRS, AVS and ZVS at the S-front are similar and close to that of aqueous sulfide right above the S-front, thus ^{34}S enriched. The formation of isotopically higher solid-phase sulfur

species is due to the reaction of ^{34}S-enriched porewater sulfide formed at depth from ^{34}S-enriched porewater sulfate (Jørgensen et al., 2004; Pellerin et al., 2018). Pyrite accumulation starts with AVS at the black band, which gradually converts into pyrite, likely via the polysulfide pathway due to the high availability of ZVS but low concentration of aqueous sulfide at the S-front (see section 4.3). This immobilization of ^{34}S-enriched aqueous sulfide as pyrite acts as an important sulfur sink as has been demonstrated by previous studies (Jørgensen et al., 2004; Holmkvist et al., 2014). Because the lacustrine sediment had only a very low Fe sulfide content, the large amounts of Fe sulfide formed today at the S-front dominate and overprint the original sulfur isotopic signature of the lacustrine sulfide minerals (Jørgensen et al., 2004). In addition, the increase in $\delta^{34}S$ of CRS from ca. 300 to 400 cmbsf results from the mixing between this newly-formed pool of ^{34}S-enriched pyrite and the large pool of ^{34}S-depleted pyrite that was previously formed close to the sediment–water interface.

The content of CRS is extremely low in the lacustrine sediments below the S-front. The $\delta^{34}S$ value of this CRS displays a negative correlation with the CRS content, suggesting a potential mixing process between two end-members (Fig. 6). Riverine sulfate has $\delta^{34}S$ values of ca. 4–6‰ (Fike et al., 2015; Burke et al., 2018). Thus, the end-member with low CRS contents and high $\delta^{34}S$ up to 6.6‰ (Fig. 6) may represent a phase formed from sulfate reduction in the sediments of the freshwaters Ancylus Lake (Calvert et al., 1996; Holmkvist et al., 2014). Recent work, however, has suggested that the sulfur isotope fractionation between sulfide and sulfate can remain large even under very low sulfate concentrations with low cell-specific sulfate reduction rates typically encountered in the environment (Wing and Halevy, 2014). Thus, it is not clear whether this pyrite was formed during lacustrine clay deposition. In contrast, a deep sulfate reservoir originating from seawater sulfate exists in the lacustrine sediments (e.g., Holmkvist et al., 2014). The presence of sulfate is also evident in dissolved barium profiles (Figs. 3C and 4C). A large portion of the barium in marine sediments is present in the form of barite, the saturation of which is dependent on porewater sulfate (e.g., Torres et al., 1996; Riedinger et al., 2006). During sediment burial, barite moves downward from sulfate-rich to sulfate-depleted porewater where it dissolves (e.g., Dickens, 2001; Monnin

et al., 2001; Henkel et al., 2012). At BB02 and BB05, dissolved barium diffuses upward and downward from sulfate-depleted to sulfate-rich porewater where it most likely precipitates as barite. Thus, the counter-directed upward flux of sulfate with extremely positive $\delta^{34}S$ suggests the occurrence of ongoing sulfate reduction in the lacustrine sediments. The $\delta^{34}S$ up to 124‰ at BB05 represent the heaviest stable sulfur isotope composition of porewater sulfate ever reported, to the best of our knowledge. The presence of sulfate-reducing bacteria and low sulfate reduction rates in lacustrine sediments from the Baltic Sea provides further supporting evidence for the metabolic capability and activity for sulfate reduction in these deeper sediments (Jochum et al., 2017; Beulig et al., 2018). Therefore, the end-member with high CRS contents and low $\delta^{34}S$ values down to −12.5‰ (Fig. 6) can be attributed to the occurrence of ongoing sulfate reduction to form more pyrite. Taken together, pyrite at the S-front was and is actively formed by recent progressive downward sulfidization, and an extremely slow pyritization in the lacustrine clay sediments is still ongoing (Holmkvist et al., 2014).

5. CONCLUSIONS

Combining sulfur isotope analyses with porewater concentrations and solid-phase abundances, we studied sediments collected at three sites in the Bornholm Basin, Baltic Sea. Rapid pyrite formation occurs close to the sediment–water interface at all investigated sites. As pyrite is growing throughout the uppermost 100 cm, the Fe_{py}/Fe_{HR} increases downcore from 0.3–0.6 near the sediment–water interface to 0.9 at around 100 cmbsf, suggesting that its use as a proxy for euxinia needs to be supported by other independent indicators in sedimentary records. The isotopic discrepancies between aqueous sulfide and solid-phase sulfur species in the subsurface sediments indicate that the bulk pools of AVS and ZVS do not exchange isotopes completely with aqueous sulfide. The surface sulfur atoms of elemental sulfur may very well be in isotopic exchange with polysulfide and, thus, with aqueous sulfide, but the bulk isotopic composition of these solid-phase sulfur species is still distinct. Moreover, as the $\delta^{34}S$ of aqueous sulfide increases with depth to values of ca. +21‰, the $\delta^{34}S$ of pyrite remains consistently at negative values, though pyrite is also forming in deeper sediments. Our diagenetic model simulates the $\delta^{34}S$ of pyrite very well, suggesting that the isotopically higher signature of the additional pyrite formed at depth is masked by the fact that most of the pyrite originates in the surface sediment with lower $\delta^{34}S$. This isotopic pattern is important because pyrite captures the isotopic signature of sulfide near the sediment–water interface despite evidence for additional accumulation of pyrite in deeper sediment. Furthermore, progressive downward sulfidization promotes pyrite formation at the sulfidization front. Concentration and sulfur isotopic composition of CRS and porewater sulfate suggest the occurrence of sulfate reduction and subsequent sluggish pyrite formation in the deep lacustrine sediments.

These results have general implications for the interpretation of iron speciation and sulfur isotopic data in both contemporary and ancient sediments with high organic matter contents, and high aqueous sulfide but low reactive iron availability. Pyrite as deep as several meters into the sediment retains the sulfur isotopic signature of the diagenesis that occurred in the upper centimeters. However, the observed isotopic pattern is not universally applicable in studies of the global sulfur cycle and should not be overinterpreted in the

ancient sedimentary record. It is likely that this pattern particularly applies to marine settings with extremely low availability of reactive iron. Additionally, sedimentation rate also plays a key role in $\delta^{34}S$ of pyrite (Pasquier et al., 2017; Liu et al., 2019). Thus, the observed diagenetic pattern differs in sedimentary environments with higher deposition rates. Although ocean chemistry has undoubtedly changed over the course of Earth's history, a contemporary understanding of early diagenetic processes remains a necessary step before the intricacies of sulfur–iron geochemical data in the geological record can be fully interpreted.

ACKNOWLEDGEMENTS

We acknowledge Susann Henkel, Ingrid Stimac, Jeanette Pedersen, Karina Bomholt Oest and Felix Beulig for their contributions and excellent technical assistance. We thank the skipper and crew of R/V *Aurora* for assistance during sampling. We also thank colleagues and students at the Center for Geomicrobiology for assistance during the research expedition and for the sampling of sediment core material. We thank Maya Gomes, Sebastiaan van de Velde and one anonymous reviewer for their helpful and constructive reviews of this paper. This work was supported by the Danish National Research Foundation (DNRF grant #104), the Danish Council for Independent Research (DFF – 7014-00196) to BBJ and the European Research Council (ERC Advanced Grant #294200). We acknowledge further financial support from the Helmholtz Association (Alfred Wegener Institute Helmholtz Centre for Polar and Marine Research in Bremerhaven). AF acknowledges a Marie-Curie European Fellowship (SedSulphOx, MSCA 746872). JL gratefully recognizes continued support and discussions from Jiasheng Wang and Tina Treude.

DECLARATION OF COMPETING INTEREST

The authors declare that they have no known competing financial interests or personal relationships that could have appeared to influence the work reported in this paper.

APPENDIX A. SUPPLEMENTARY MATERIAL

Research data associated with this article are included in the supplementary material.

TABLE and FIGURES

Table 1

Location of sampling sites in the Bornholm Basin (Beulig et al., 2018), as well as information on the water depth, sedimentation rates (ω), Holocene Mud Layer (HML) thickness and depth of the sulfate–methane transition (SMT; mbsf = meters below seafloor).

Site	Latitude/longitude	Water depth (m)	ω (cm y^{-1})	HML (m)	SMT (mbsf)
BB01	55°22.922′N / 15°27.675′E	96	0.065	5.5	0.6
BB02	55°23.281′N / 15°28.004′E	96	0.053	4.5	0.7
BB05	55°24.418′N / 15°28.550′E	95	0.049	4.2	3.7

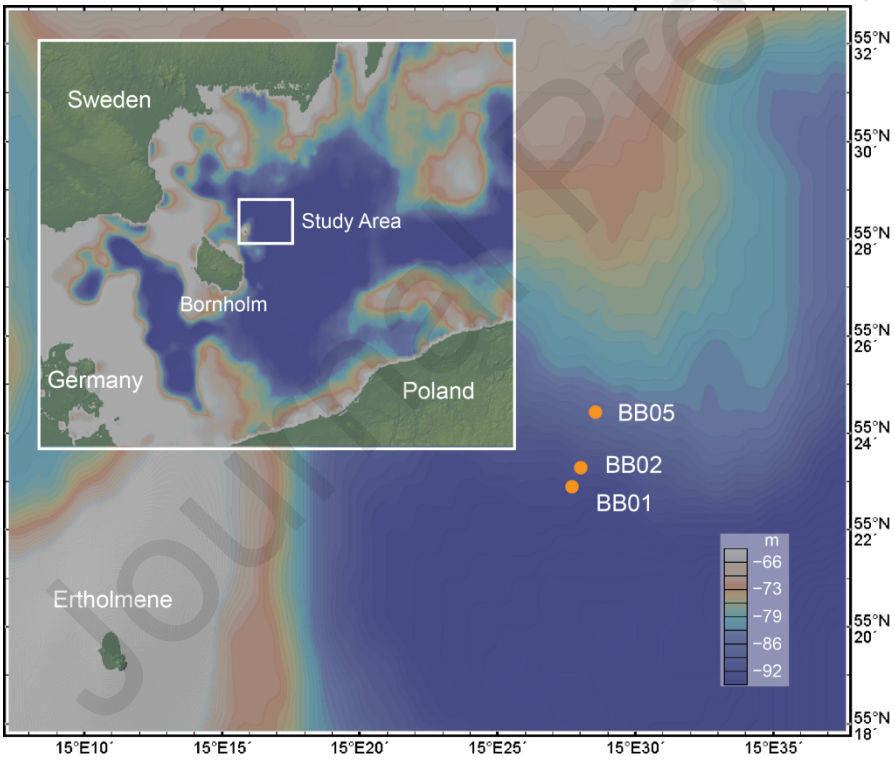

Fig. 1. Map of the study sites in the Bornholm Basin of the southwestern Baltic Sea. The map was generated using GeoMapApp.

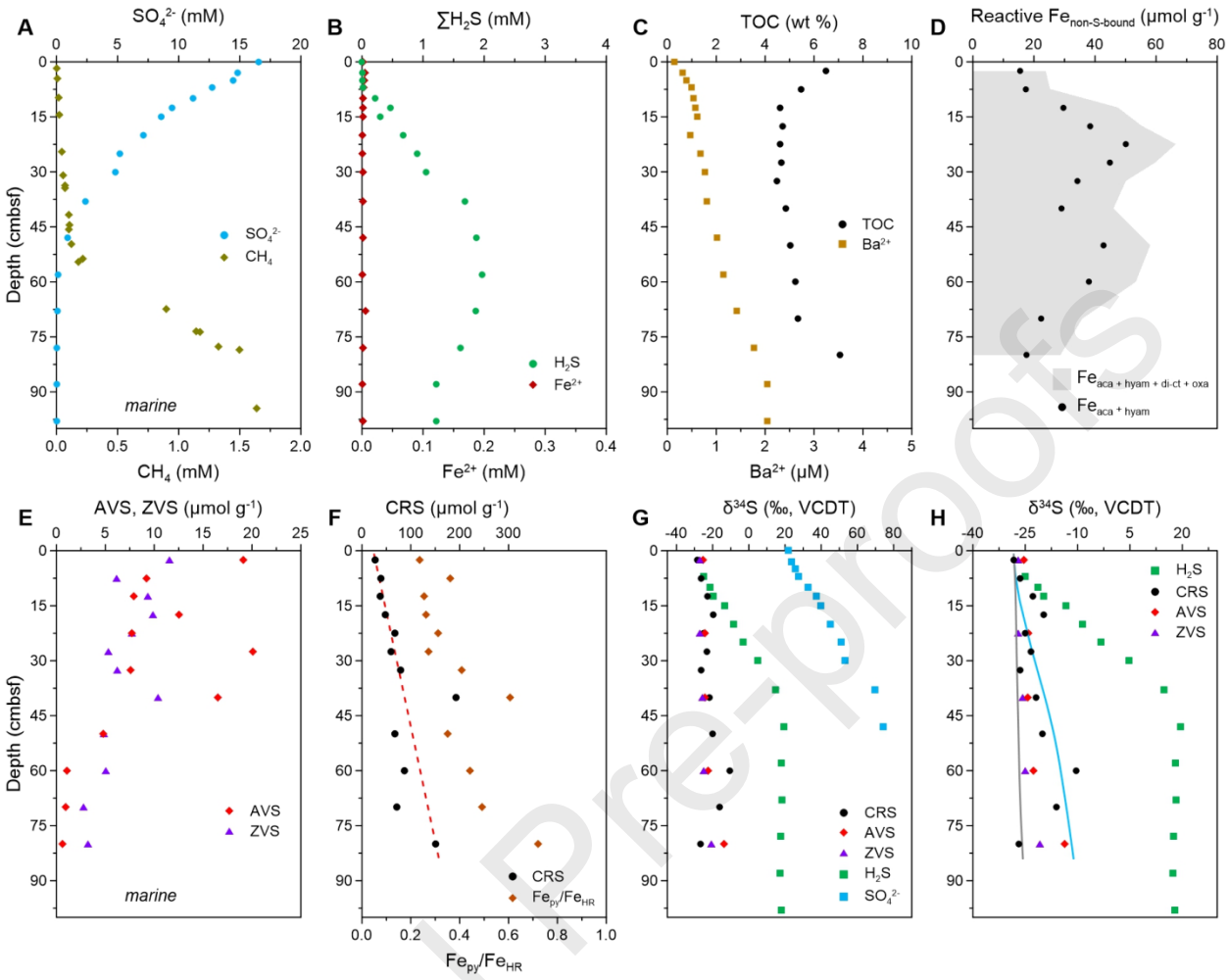

Fig. 2. Geochemical depth profiles for site BB01. (A) Porewater sulfate and methane. (B) Porewater sulfide and dissolved ferrous iron. (C) Total organic carbon and porewater barium. (D) Non-sulfur-bound reactive iron. Results using two definitions are shown for comparison. (E) Acid volatile sulfur and zero-valent sulfur. (F) Chromium reducible sulfur and the extent of pyritization of the highly reactive iron pool. (G) Isotopic composition of sulfur species. (H) Isotopic composition of sulfur species with the results of the diagenetic model. The red line in F shows a constant rate of pyrite formation used in the model. The solid blue and grey lines in panel H represent the simulated $\delta^{34}S$ values of pyrite formed via the H_2S pathway and the polysulfide pathway, respectively. For Figs. 2–4, solid-phase sulfur and iron data are expressed relative to the wet mass of the sample, while contents of TOC are reported on a dry weight basis.

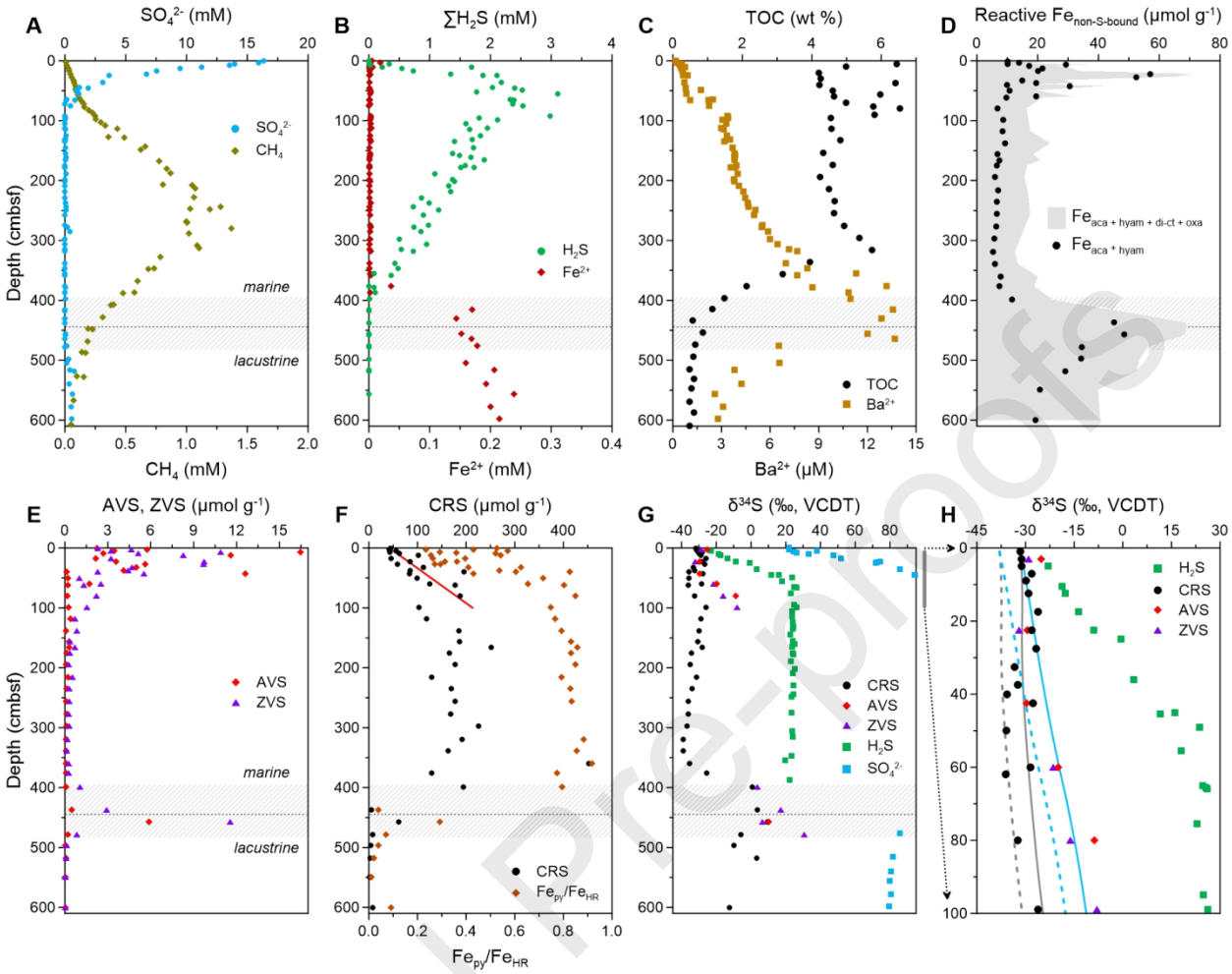

Fig. 3. Geochemical depth profiles for site BB02. (A) Porewater sulfate and methane. (B) Porewater sulfide and dissolved ferrous iron. (C) Total organic carbon and porewater barium. (D) Non-sulfur-bound reactive iron. Results using two definitions are shown for comparison. (E) Acid volatile sulfur and zero-valent sulfur. (F) Chromium reducible sulfur and the extent of pyritization of the highly reactive iron pool. (G) Isotopic composition of sulfur species throughout the core. (H) Isotopic composition of sulfur species with the results of the diagenetic model in the near-surface sediment. The red line in F shows a constant rate of pyrite formation used in the model. The solid blue and grey lines in panel H represent the simulated $\delta^{34}S$ values of pyrite formed via the H_2S pathway and the polysulfide pathway, respectively. The dashed lines in H depict an alternative scenario in which pyrite originating from the sediment surface has a lower $\delta^{34}S$. The horizontal bars and dashed lines represent the sulfidization front and the marine–lacustrine transition, respectively. It should be noted that the depth axes of panel G and H are not on the same scale.

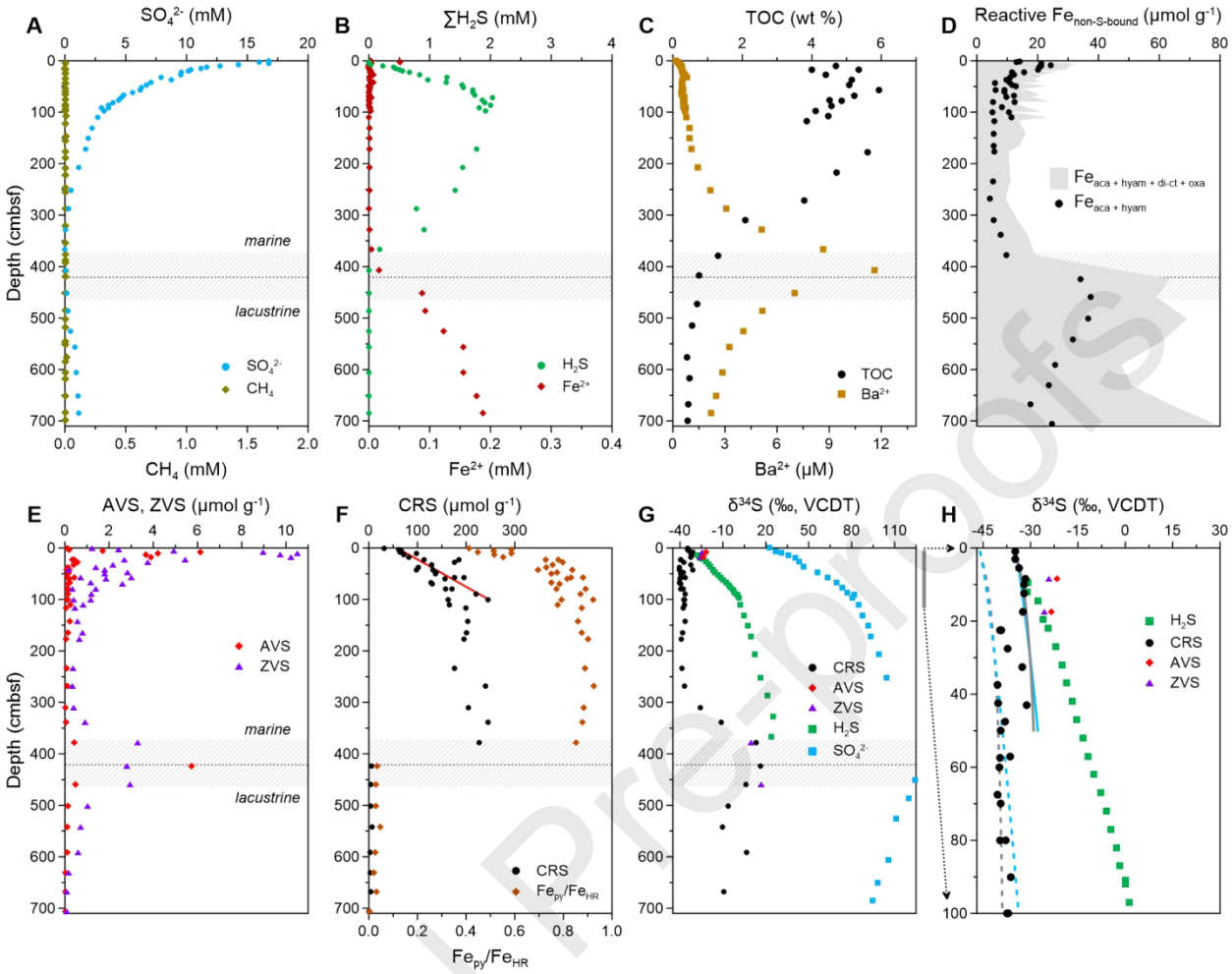

Fig. 4. Geochemical depth profiles for site BB05. (A) Porewater sulfate and methane. (B) Porewater sulfide and dissolved ferrous iron. (C) Total organic carbon and porewater barium. (D) Non-sulfur-bound reactive iron. (E) Acid volatile sulfur and zero-valent sulfur. (F) Chromium reducible sulfur and the extent of pyritization of the highly reactive iron pool. (G) Isotopic composition of sulfur species throughout the core. (H) Isotopic composition of sulfur species with the results of the diagenetic model in the near-surface sediment. Legends follow Fig. 3.

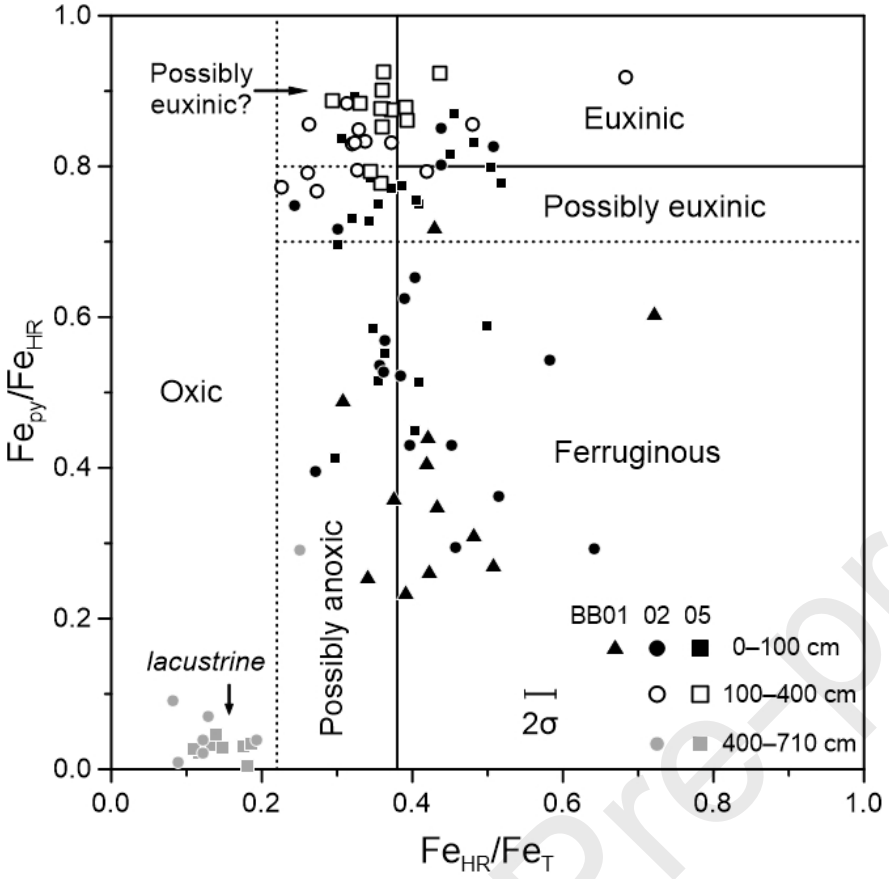

Fig. 5. Cross-plot of the ratios of pyrite Fe to highly reactive Fe against highly reactive Fe to total Fe. Horizontal and vertical lines indicate the proposed boundaries for distinguishing euxinic from anoxic and iron-rich (ferruginous) from oxic water columns (cf. Li et al., 2010; Poulton and Canfield, 2011; Raiswell et al., 2018). Fe_T is assumed to be constant with a standard deviation (2σ) from Dijkstra et al. (2018) due to lack of stratigraphic variation in the Bornholm Basin.

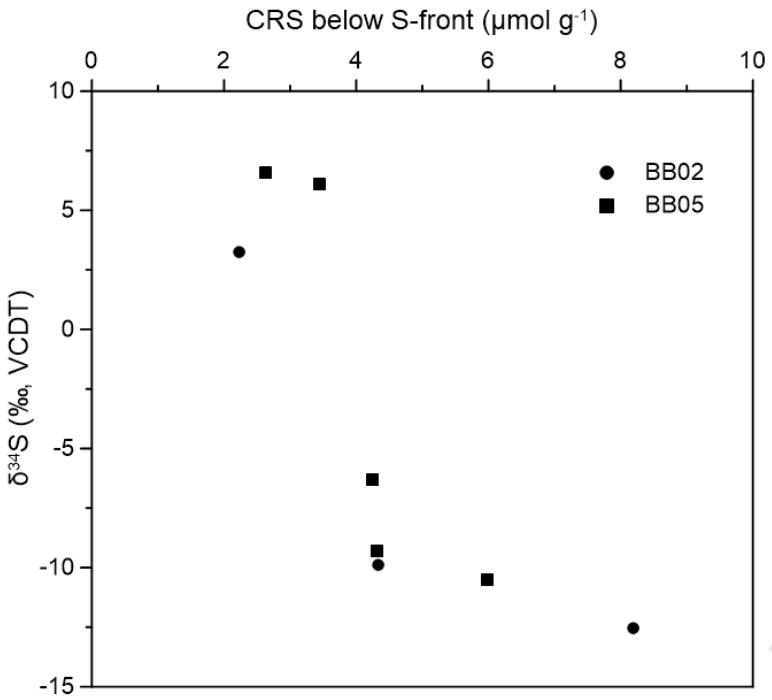

Fig. 6. Content of chromium reducible sulfur versus its $\delta^{34}S$ value in the deep lacustrine clay (below the sulfidization front) at sites BB02 and BB05.

REFERENCES

Algeo T.J. and Li C. (2020) Redox classification and calibration of redox thresholds in sedimentary systems. *Geochim. Cosmochim. Ac.*

Anderson T.F. and Raiswell R. (2004) Sources and mechanisms for the enrichment of highly reactive iron in euxinic Black Sea sediments. *Am. J. Sci.* **304**, 203-233.

Andrén E., Andrén T. and Sohlenius G. (2000) The Holocene history of the southwestern Baltic Sea as reflected in a sediment core from the Bornholm Basin. *Boreas* **29**, 233-250.

Andrén T., Jørgensen B.B., Cotterill C., Green S. and Expedition 347 Scientists (2015) Site M0065. In Proc. IODP, 347: College Station, TX (Integrated Ocean Drilling Program).

Bennett W.W. and Canfield D.E. (2020) Redox-sensitive trace metals as paleoredox proxies: A review and analysis of data from modern sediments. *Earth-Sci. Rev.* **204**, 103175.

Berner R.A. (1984) Sedimentary pyrite formation: An update. *Geochim. Cosmochim. Ac.* **48**, 605-615.

Beulig F., Røy H., Glombitza C. and Jørgensen B.B. (2018) Control on rate and pathway of anaerobic organic carbon degradation in the seabed. *P. Natl. Acad. Sci. USA* **115**, 367-372.

Boesen C. and Postma D. (1988) Pyrite formation in anoxic environments of the Baltic. *Am. J. Sci.* **288**, 575-603.

Borowski W.S., Rodriguez N.M., Paull C.K. and Ussler III W. (2013) Are ^{34}S-enriched authigenic sulfide minerals a proxy for elevated methane flux and gas hydrates in the geologic record? *Mar. Pet. Geol.* **43**, 381-395.

Böttcher M.E. and Lepland A. (2000) Biogeochemistry of sulfur in a sediment core from the west-central Baltic Sea: Evidence from stable isotopes and pyrite textures. *J. Mar. Syst.* **25**, 299-312.

Böttcher M.E., Thamdrup B. and Vennemann T.W. (2001) Oxygen and sulfur isotope fractionation during anaerobic bacterial disproportionation of elemental sulfur. *Geochim. Cosmochim. Ac.* **65**, 1601-1609.

Bottrell S.H. and Newton R.J. (2006) Reconstruction of changes in global sulfur cycling from marine sulfate isotopes. *Earth-Sci. Rev.* **75**, 59-83.

Brüchert V., Pratt L.M., Anderson T.F. and Hoffmann S.R. (1995) Abundance and isotopic composition of organic and inorganic sulfur species in laminated and bioturbated sediments from Hole 893A, Santa Barbara Basin. In Proceedings of the Ocean Drilling Program, Scientific Results, vol. 146 (eds. J. P. Kennett, J. G. Baldauf and M. Lyle), pp. 219–230.

Burke A., Present T.M., Paris G., Rae E.C.M., Sandilands B.H., Gaillardet J., Peucker-Ehrenbrink B., Fischer W.W., McClelland J.W., Spencer R.G.M., Voss B.M. and Adkins J.F. (2018) Sulfur isotopes in rivers: Insights into global weathering budgets, pyrite oxidation, and the modern sulfur cycle. *Earth. Planet. Sci. Lett.* **496**, 168-177.

Butler I.B., Böttcher M.E., Rickard D. and Oldroyd A. (2004) Sulfur isotope partitioning during experimental formation of pyrite via the polysulfide and hydrogen sulfide pathways: implications for the interpretation of sedimentary and hydrothermal pyrite isotope records. *Earth. Planet. Sci. Lett.* **228**, 495-509.

Calvert S.E., Thode H.G., Yeung D. and Karlin R.E. (1996) A stable isotope study of pyrite formation in the Late Pleistocene and Holocene sediments of the Black Sea. *Geochim. Cosmochim. Ac.* **60**, 1261-1270.

Canfield D. and Thamdrup B. (1994) The production of ^{34}S-depleted sulfide during bacterial disproportionation of elemental sulfur. *Science* **266**, 1973-1975.

Canfield D.E. (1989) Reactive iron in marine sediments. *Geochim. Cosmochim. Ac.* **53**, 619-632.

Canfield D.E. (2001) Biogeochemistry of Sulfur Isotopes. *Rev. Mineral Geochem.* **43**, 607-636.

Canfield D.E., Lyons T.W. and Raiswell R. (1996) A model for iron deposition to euxinic Black Sea sediments. *Am. J. Sci.* **296**, 818-834.

Canfield D.E., Raiswell R. and Bottrell S.H. (1992) The reactivity of sedimentary iron minerals toward sulfide. *Am. J. Sci.* **292**, 659-683.

Carstensen J., Andersen J.H., Gustafsson B.G. and Conley D.J. (2014) Deoxygenation of the Baltic Sea during the last century. *P. Natl. Acad. Sci. USA* **111**, 5628-5633.

Chanton J.P., Martens C.S. and Goldhaber M.B. (1987) Biogeochemical cycling in an organic-rich coastal marine basin. 8. A sulfur isotopic budget balanced by differential diffusion across the sediment-water interface. *Geochim. Cosmochim. Ac.* **51**, 1201-1208.

Chester R. and Hughes M.J. (1967) A chemical technique for the separation of ferro-manganese minerals, carbonate minerals and adsorbed trace elements from pelagic sediments. *Chem. Geol.* **2**, 249-262.

Cline J.D. (1969) Spectrophotometric determination of hydrogen sulfide in natural waters. *Limnol. Oceanogr.* **14**, 454-458.

Conley D.J., Björck S., Bonsdorff E., Carstensen J., Destouni G., Gustafsson B.G., Hietanen S., Kortekaas M., Kuosa H., Markus Meier H.E., Müller-Karulis B., Nordberg K., Norkko A., Nürnberg G., Pitkänen H., Rabalais N.N., Rosenberg R., Savchuk O.P., Slomp C.P., Voss M., Wulff F. and Zillén L. (2009) Hypoxia-Related Processes in the Baltic Sea. *Environ. Sci. Technol.* **43**, 3412-3420.

Dickens G.R. (2001) Sulfate profiles and barium fronts in sediment on the Blake Ridge: present and past methane fluxes through a large gas hydrate reservoir. *Geochim. Cosmochim. Ac.* **65**, 529-543.

Dijkstra N., Hagens M., Egger M. and Slomp C.P. (2018) Post-depositional formation of vivianite-type minerals alters sediment phosphorus records. *Biogeosciences* **15**, 861-883.

Fike D.A., Bradley A.S. and Rose C.V. (2015) Rethinking the ancient sulfur cycle. *Annu. Rev. Earth Pl. Sc.* **43**, 593-622.

Findlay A.J. (2016) Microbial impact on polysulfide dynamics in the environment. *FEMS Microbiol. Lett.* **363**, fnw103.

Findlay A.J., Gartman A., MacDonald D.J., Hanson T.E., Shaw T.J. and Luther G.W. (2014) Distribution and size fractionation of elemental sulfur in aqueous environments: the Chesapeake Bay and Mid-Atlantic Ridge. *Geochim. Cosmochim. Ac.* **142**, 334-348.

Findlay A.J., Pellerin A., Laufer K. and Barker Jørgensen B. (2020) Quantification of sulphide oxidation rates in marine sediment. *Geochim. Cosmochim. Ac.*

Fonselius S. (1981) Oxygen and hydrogen sulphide conditions in the Baltic Sea. *Mar. Pollut. Bull.* **12**, 187-194.

Formolo M.J. and Lyons T.W. (2013) Sulfur biogeochemistry of cold seeps in the Green Canyon region of the Gulf of Mexico. *Geochim. Cosmochim. Ac.* **119**, 264-285.

Fossing H. and Jørgensen B.B. (1989) Measurement of bacterial sulfate reduction in sediments: evaluation of a single-step chromium reduction method. *Biogeochemistry* **8**, 205-222.

Fossing H. and Jørgensen B.B. (1990) Isotope exchange reactions with radiolabeled sulfur compounds in anoxic seawater. *Biogeochemistry* **9**, 223-245.

Fossing H., Thode-Andersen S. and Jørgensen B.B. (1992) Sulfur isotope exchange between ^{35}S-labeled inorganic sulfur compounds in anoxic marine sediments. *Mar. Chem.* **38**, 117-132.

Fry B., Cox J., Gest H. and Hayes J. (1986) Discrimination between ^{34}S and ^{32}S during bacterial metabolism of inorganic sulfur compounds. *J. Bacteriol.* **165**, 328-330.

Fu Y., von Dobeneck T., Franke C., Heslop D. and Kasten S. (2008) Rock magnetic identification and geochemical process models of greigite formation in Quaternary marine sediments from the Gulf of Mexico (IODP Hole U1319A). *Earth. Planet. Sci. Lett.* **275**, 233-245.

Habicht K.S. and Canfield D.E. (1997) Sulfur isotope fractionation during bacterial sulfate reduction in organic-rich sediments. *Geochim. Cosmochim. Ac.* **61**, 5351-5361.

Habicht K.S. and Canfield D.E. (2001) Isotope fractionation by sulfate-reducing natural populations and the isotopic composition of sulfide in marine sediments. *Geology* **29**, 555-558.

Hardisty D.S., Lyons T.W., Riedinger N., Isson T.T., Owens J.D., Aller R.C., Rye D.M., Planavsky N.J., Reinhard C.T., Gill B.C., Masterson A.L., Asael D. and Johnston D.T. (2018) An Evaluation of Sedimentary Molybdenum and Iron as Proxies for Pore Fluid Paleoredox Conditions. *Am. J. Sci.* **318**, 527-556.

Henkel S., Kasten S., Poulton S.W. and Staubwasser M. (2016) Determination of the stable iron isotopic composition of sequentially leached iron phases in marine sediments. *Chem. Geol.* **421**, 93-102.

Henkel S., Mogollón J.M., Nöthen K., Franke C., Bogus K., Robin E., Bahr A., Blumenberg M., Pape T., Seifert R., März C., de Lange G.J. and Kasten S. (2012) Diagenetic barium cycling in Black Sea sediments – A case study for anoxic marine environments. *Geochim. Cosmochim. Ac.* **88**, 88-105.

Hensen C., Zabel M., Pfeifer K., Schwenk T., Kasten S., Riedinger N., Schulz H.D. and Boetius A. (2003) Control of sulfate pore-water profiles by sedimentary events and the significance of anaerobic oxidation of methane for the burial of sulfur in marine sediments. *Geochim. Cosmochim. Ac.* **67**, 2631-2647.

Hermans M., Lenstra W.K., Hidalgo-Martinez S., van Helmond N.A.G.M., Witbaard R., Meysman F.J.R., Gonzalez S. and Slomp C.P. (2019) Abundance and Biogeochemical Impact of Cable Bacteria in Baltic Sea Sediments. *Environ. Sci. Technol.* **53**, 7494-7503.

Hilligsøe K.M., Jensen J.B., Ferdelman T.G., Fossing H., Lapham L., Røy H. and Jørgensen B.B. (2018) Methane fluxes in marine sediments quantified through core analyses and seismo-acoustic mapping (Bornholm Basin, Baltic Sea). *Geochim. Cosmochim. Ac.* **239**, 255-274.

Holmkvist L., Ferdelman T.G. and Jørgensen B.B. (2011) A cryptic sulfur cycle driven by iron in the methane zone of marine sediment (Aarhus Bay, Denmark). *Geochim. Cosmochim. Ac.* **75**, 3581-3599.

Holmkvist L., Kamyshny Jr A., Bruechert V., Ferdelman T.G. and Jørgensen B.B. (2014) Sulfidization of lacustrine glacial clay upon Holocene marine transgression (Arkona Basin, Baltic Sea). *Geochim. Cosmochim. Ac.* **142**, 75-94.

Jensen J.B. and Endler R. (2012) Methane distribution in Holocene marine sediments in the Bornholm Basin, southern Scandinavia. *Geol. Surv. Denmark Greenland Bull.* **26**, 21–24.

Jensen J.B., Moros M., Endler R. and Members I.E. (2017) The Bornholm Basin, southern Scandinavia: a complex history from Late Cretaceous structural developments to recent sedimentation. *Boreas* **46**, 3-17.

Jochum L.M., Chen X., Lever M.A., Loy A., Jørgensen B.B., Schramm A. and Kjeldsen K.U. (2017) Depth distribution and assembly of sulfate-reducing microbial communities in marine sediments of Aarhus Bay. *Appl. Environ. Microbiol.* **83**, e01547-01517.

Jørgensen B.B. (1978) A comparison of methods for the quantification of bacterial sulfate reduction in coastal marine sediments. *Geomicrobiol. J.* **1**, 49-64.

Jørgensen B.B. (1979) A theoretical model of the stable sulfur isotope distribution in marine sediments. *Geochim. Cosmochim. Ac.* **43**, 363-374.

Jørgensen B.B. (1982) Mineralization of organic matter in the sea bed—the role of sulphate reduction. *Nature* **296**, 643-645.

Jørgensen B.B., Böttcher M.E., Lüschen H., Neretin L.N. and Volkov I.I. (2004) Anaerobic methane oxidation and a deep H_2S sink generate isotopically heavy sulfides in Black Sea sediments. *Geochim. Cosmochim. Ac.* **68**, 2095-2118.

Jørgensen B.B., Findlay A.J. and Pellerin A. (2019) The biogeochemical sulfur cycle of marine sediments. *Front. Microbiol.* **10**, 849.

Jørgensen B.B. and Kasten S. (2006) Sulfur cycling and methane oxidation, in: Schulz, H.D., Zabel, M. (Eds.), Marine Geochemistry. Springer Berlin Heidelberg, Berlin, Heidelberg, pp. 271-309.

Kamyshny A. and Ferdelman T.G. (2010) Dynamics of zero-valent sulfur species including polysulfides at seep sites on intertidal sand flats (Wadden Sea, North Sea). *Mar. Chem.* **121**, 17-26.

Kaplan I.R., Emery K.O. and Rittenbebg S.C. (1963) The distribution and isotopic abundance of sulphur in recent marine sediments off southern California. *Geochim. Cosmochim. Ac.* **27**, 297-331.

Kasten S., Freudenthal T., Gingele F.X. and Schulz H.D. (1998) Simultaneous formation of iron-rich layers at different redox boundaries in sediments of the Amazon deep-sea fan. *Geochim. Cosmochim. Ac.* **62**, 2253-2264.

Laufer K., Michaud A.B., Røy H. and Jørgensen B.B. (2020) Reactivity of Iron Minerals in the Seabed Toward Microbial Reduction – A Comparison of Different Extraction Techniques. *Geomicrobiol. J.* **37**, 170-189.

Leavitt W.D., Halevy I., Bradley A.S. and Johnston D.T. (2013) Influence of sulfate reduction rates on the Phanerozoic sulfur isotope record. *P. Natl. Acad. Sci. USA* **110**, 11244-11249.

Li C., Love G.D., Lyons T.W., Fike D.A., Sessions A.L. and Chu X. (2010) A Stratified Redox Model for the Ediacaran Ocean. *Science* **328**, 80-83.

Lin Q., Wang J., Fu S., Lu H., Bu Q., Lin R. and Sun F. (2015) Elemental sulfur in northern South China Sea sediments and its significance. *Sci. China Earth Sci.* **58**, 2271-2278.

Lin Z., Sun X., Peckmann J., Lu Y., Xu L., Strauss H., Zhou H., Gong J., Lu H. and Teichert B.M.A. (2016) How sulfate-driven anaerobic oxidation of methane affects the sulfur isotopic composition of pyrite: A SIMS study from the South China Sea. *Chem. Geol.* **440**, 26-41.

Liu J., Pellerin A., Izon G., Wang J., Antler G., Liang J., Su P., Jørgensen B.B. and Ono S. (2020) The multiple sulphur isotope fingerprint of a sub-seafloor oxidative sulphur cycle driven by iron. *Earth. Planet. Sci. Lett.* **536**, 116165.

Liu X., Fike D., Li A., Dong J., Xu F., Zhuang G., Rendle-Bühring R. and Wan S. (2019) Pyrite sulfur isotopes constrained by sedimentation rates: Evidence from sediments on the East China Sea inner shelf since the late Pleistocene. *Chem. Geol.* **505**, 66-75.

Luther G.W. (1991) Pyrite synthesis via polysulfide compounds. *Geochim. Cosmochim. Ac.* **55**, 2839-2849.

Lyons T.W., Anbar A.D., Severmann S., Scott C. and Gill B.C. (2009) Tracking Euxinia in the Ancient Ocean: A Multiproxy Perspective and Proterozoic Case Study. *Annu. Rev. Earth Pl. Sc.* **37**, 507-534.

Lyons T.W. and Severmann S. (2006) A critical look at iron paleoredox proxies: New insights from modern euxinic marine basins. *Geochim. Cosmochim. Ac.* **70**, 5698-5722.

März C., Poulton S.W., Beckmann B., Küster K., Wagner T. and Kasten S. (2008a) Redox sensitivity of P cycling during marine black shale formation: Dynamics of sulfidic and anoxic, non-sulfidic bottom waters. *Geochim. Cosmochim. Ac.* **72**, 3703-3717.

März C., Hoffmann J., Bleil U., De Lange G. and Kasten S. (2008b) Diagenetic changes of magnetic and geochemical signals by anaerobic methane oxidation in sediments of the Zambezi deep-sea fan (SW Indian Ocean). *Mar. Geol.* **255**, 118-130.

Middelburg J.J. (1991) Organic carbon, sulphur, and iron in recent semi-euxinic sediments of Kau Bay, Indonesia. *Geochim. Cosmochim. Ac.* **55**, 815-828.

Monnin C., Wheat C.G., Dupre B., Elderfield H. and Mottl M.M. (2001) Barium geochemistry in sediment pore waters and formation waters of the oceanic crust on the eastern flank of the Juan de Fuca Ridge (ODP Leg 168). *Geochem. Geophys. Geosyst.* **2**, 1008.

Moros M., Lemke W., Kuijpers A., Endler R., Jensen J.B., Bennike O. and Gingele F. (2002) Regressions and transgressions of the Baltic basin reflected by a new high-resolution deglacial and postglacial lithostratigraphy for Arkona Basin sediments (western Baltic Sea). *Boreas* **31**, 151-162.

Neretin L.N., Böttcher M.E., Jørgensen B.B., Volkov I.I., Lüschen H. and Hilgenfeldt K. (2004) Pyritization processes and greigite formation in the advancing sulfidization front in the upper Pleistocene sediments of the Black Sea. *Geochim. Cosmochim. Ac.* **68**, 2081-2093.

Oni O., Miyatake T., Kasten S., Richter-Heitmann T., Fischer D., Wagenknecht L., Ksenofontov V., Kulkarni A., Blumers M., Shylin S., Costa B., Klingelhöfer G. and Friedrich M. (2015) Distinct microbial populations are tightly linked to the profile of dissolved iron in the methanic sediments of the Helgoland mud area, North Sea. *Front. Microbiol.* **6**, 365.

Pasquier V., Sansjofre P., Rabineau M., Revillon S., Houghton J. and Fike D.A. (2017) Pyrite sulfur isotopes reveal glacial−interglacial environmental changes. *P. Natl. Acad. Sci. USA* **114**, 5941-5945.

Peiffer S., Behrends T., Hellige K., Larese-Casanova P., Wan M. and Pollok K. (2015) Pyrite formation and mineral transformation pathways upon sulfidation of ferric hydroxides depend on mineral type and sulfide concentration. *Chem. Geol.* **400**, 44-55.

Pellerin A., Antler G., Holm S.A., Findlay A.J., Crockford P.W., Turchyn A.V., Jørgensen B.B. and Finster K. (2019) Large sulfur isotope fractionation by bacterial sulfide oxidation. *Sci. Adv.* **5**, eaaw1480.

Pellerin A., Antler G., Røy H., Findlay A., Beulig F., Scholze C., Turchyn A.V. and Barker Jørgensen B. (2018) The sulfur cycle below the sulfate-methane transition of marine sediments. *Geochim. Cosmochim. Ac.* **239**, 74-89.

Poulton S.W. and Canfield D.E. (2005) Development of a sequential extraction procedure for iron: implications for iron partitioning in continentally derived particulates. *Chem. Geol.* **214**, 209-221.

Poulton S.W. and Canfield D.E. (2011) Ferruginous Conditions: A Dominant Feature of the Ocean through Earth's History. *Elements* **7**, 107-112.

Poulton S.W., Krom M.D. and Raiswell R. (2004) A revised scheme for the reactivity of iron (oxyhydr) oxide minerals towards dissolved sulfide. *Geochim. Cosmochim. Ac.* **68**, 3703-3715.

Poulton S.W. and Raiswell R. (2002) The low-temperature geochemical cycle of iron: From continental fluxes to marine sediment deposition. *Am. J. Sci.* **302**, 774-805.

Raiswell R., Buckley F., Berner R.A. and Anderson T.F. (1988) Degree of pyritization of iron as a paleoenvironmental indicator of bottom-water oxygenation. *J. Sediment. Res.* **58**, 812-819.

Raiswell R., Canfield D. and Berner R. (1994) A comparison of iron extraction methods for the determination of degree of pyritisation and the recognition of iron-limited pyrite formation. *Chem. Geol.* **111**, 101-110.

Raiswell R. and Canfield D.E. (1998) Sources of iron for pyrite formation in marine sediments. *Am. J. Sci.* **298**, 219-245.

Raiswell R. and Canfield D.E. (2012) The iron biogeochemical cycle past and present. *Geochem. Perspect.* **1**, 19-41.

Raiswell R., Hardisty D.S., Lyons T.W., Canfield D.E., Owens J.D., Planavsky N.J., Poulton S.W. and Reinhard C.T. (2018) The iron paleoredox proxies: A guide to the pitfalls, problems and proper practice. *Am. J. Sci.* **318**, 491-526.

Raven M.R., Sessions A.L., Fischer W.W. and Adkins J.F. (2016) Sedimentary pyrite $\delta^{34}S$ differs from porewater sulfide in Santa Barbara Basin: Proposed role of organic sulfur. *Geochim. Cosmochim. Ac.* **186**, 120-134.

Rickard D. (1995) Kinetics of FeS precipitation: Part 1. Competing reaction mechanisms. *Geochim. Cosmochim. Ac.* **59**, 4367-4379.

Rickard D. (1997) Kinetics of pyrite formation by the H_2S oxidation of iron (II) monosulfide in aqueous solutions between 25 and 125°C: The rate equation. *Geochim. Cosmochim. Ac.* **61**, 115-134.

Rickard D. (2012a) Euxinic Systems, in: Rickard, D. (Ed.), Developments in Sedimentology. Elsevier, pp. 495-542.

Rickard D. (2012b) Microbial Sulfide Oxidation in Sediments, in: Rickard, D. (Ed.), Developments in Sedimentology. Elsevier, pp. 353-372.

Rickard D. and Luther G.W. (2007) Chemistry of Iron Sulfides. *Chem. Rev.* **107**, 514-562.

Rickard D. and Morse J.W. (2005) Acid volatile sulfide (AVS). *Mar. Chem.* **97**, 141-197.

Rickard D.T. (1975) Kinetics and mechanism of pyrite formation at low temperatures. *Am. J. Sci.* **275**, 636-652.

Riedinger N., Brunner B., Krastel S., Arnold G.L., Wehrmann L.M., Formolo M.J., Beck A., Bates S.M., Henkel S. and Kasten S. (2017) Sulfur cycling in an iron oxide-dominated, dynamic marine depositional system: The Argentine continental margin. *Front. Earth Sci.* **5**, 33.

Riedinger N., Formolo M.J., Lyons T.W., Henkel S., Beck A. and Kasten S. (2014) An inorganic geochemical argument for coupled anaerobic oxidation of methane and iron reduction in marine sediments. *Geobiology* **12**, 172-181.

Riedinger N., Kasten S., Gröger J., Franke C. and Pfeifer K. (2006) Active and buried authigenic barite fronts in sediments from the Eastern Cape Basin. *Earth. Planet. Sci. Lett.* **241**, 876-887.

Riedinger N., Pfeifer K., Kasten S., Garming J.F.L., Vogt C. and Hensen C. (2005) Diagenetic alteration of magnetic signals by anaerobic oxidation of methane related to a change in sedimentation rate. *Geochim. Cosmochim. Ac.* **69**, 4117-4126.

Roberts A.P. (2015) Magnetic mineral diagenesis. *Earth-Sci. Rev.* **151**, 1-47.

Shawar L., Halevy I., Said-Ahmad W., Feinstein S., Boyko V., Kamyshny A. and Amrani A. (2018) Dynamics of pyrite formation and organic matter sulfurization in organic-rich carbonate sediments. *Geochim. Cosmochim. Ac.* **241**, 219-239.

Sim M.S., Bosak T. and Ono S. (2011) Large Sulfur Isotope Fractionation Does Not Require Disproportionation. *Science* **333**, 74-77.

Slotznick S.P., Sperling E.A., Tosca N.J., Miller A.J., Clayton K.E., van Helmond N.A.G.M., Slomp C.P. and Swanson-Hysell N.L. (2020) Unraveling the Mineralogical Complexity of Sediment Iron Speciation Using Sequential Extractions. *Geochem. Geophys. Geosyst.* **21**, e2019GC008666.

Sohlenius G., Emeis K.C., Andrén E., Andrén T. and Kohly A. (2001) Development of anoxia during the Holocene fresh–brackish water transition in the Baltic Sea. *Mar. Geol.* **177**, 221-242.

Sternbeck J. and Sohlenius G. (1997) Authigenic sulfide and carbonate mineral formation in Holocene sediments of the Baltic Sea. *Chem. Geol.* **135**, 55-73.

Thamdrup B., Fossing H. and Jørgensen B.B. (1994) Manganese, iron and sulfur cycling in a coastal marine sediment, Aarhus bay, Denmark. *Geochim. Cosmochim. Ac.* **58**, 5115-5129.

Thiel J., Byrne J.M., Kappler A., Schink B. and Pester M. (2019) Pyrite formation from FeS and H_2S is mediated through microbial redox activity. *P. Natl. Acad. Sci. USA* **116**, 6897-6902.

Torres M.E., Brumsack H.J., Bohrmann G. and Emeis K.C. (1996) Barite fronts in continental margin sediments: a new look at barium remobilization in the zone of sulfate reduction and formation of heavy barites in diagenetic fronts. *Chem. Geol.* **127**, 125-139.

Turchyn A.V., Antler G., Byrne D., Miller M. and Hodell D.A. (2016) Microbial sulfur metabolism evidenced from pore fluid isotope geochemistry at Site U1385. *Global Planet. Change* **141**, 82-90.

Wan M., Schröder C. and Peiffer S. (2017) Fe(III):S(-II) concentration ratio controls the pathway and the kinetics of pyrite formation during sulfidation of ferric hydroxides. *Geochim. Cosmochim. Ac.* **217**, 334-348.

Wing B.A. and Halevy I. (2014) Intracellular metabolite levels shape sulfur isotope fractionation during microbial sulfate respiration. *P. Natl. Acad. Sci. USA* **111**, 18116-18125.

Yücel M., Luther G.W. and Moore W.S. (2010) Earthquake-induced turbidite deposition as a previously unrecognized sink for hydrogen sulfide in the Black Sea sediments. *Mar. Chem.* **121**, 176-186.

Zopfi J., Böttcher M.E. and Jørgensen B.B. (2008) Biogeochemistry of sulfur and iron in Thioploca-colonized surface sediments in the upwelling area off central chile. *Geochim. Cosmochim. Ac.* **72**, 827-843.

Zopfi J., Ferdelmann T. and Fossing H. (2004) Distribution and fate of sulfur intermediates-sulfite, tetrathionate, thiosulfate, and elemental sulfur-in marine sediments, in: Amend, J.P., Edwards, K.J., Lyons, T.W. (Eds.), Sulfur Biogeochemistry - Past and Present. Geological Society of America, Colorado, USA, pp. 97-116.